Citation
Crossley, R.J. and Evans, K.A. and Evans, N.J. and Bragagni, A. and McDonald, B.J. and Reddy, S.M. and Speelmanns, I.M. 2020. Tracing highly siderophile elements through subduction: Insights from high-pressure serpentinites and 'hybrid' rocks from alpine corsica. Journal of Petrology. 61 (2): ARTN egaa030. http://doi.org/10.1093/petrology/egaa030

Tracing highly siderophile elements through subduction: Insights from high-pressure serpentinites and 'hybrid' rocks from Alpine Corsica

R.J. Crossley[1]*, K.A. Evans[1], N.J. Evans[1,2], A. Bragagni[3,4], B.J. McDonald[1,2], S. M. Reddy[1], & I.M. Speelmanns[4,5]

[1] School of Earth and Planetary Sciences, The Institute for Geoscience Research (TIGeR), Curtin University, GPO Box U1987, Perth, WA 6845, Australia.

[2]John de Laeter Centre, Curtin University, GPO Box U1987, Perth, WA 6845, Australia.

[3] Steinmann-Institut für Edogene Prozesse, Universität Bonn, Poppelsdorfer Schloß, 53115 Bonn, Germany.

[4] Institut für Geologie und Mineralogie, Universität zu Köln, Greinstr. 4-6, D-50937 Köln, Germany.

[5]Institute for Geochemistry and Petrology, ETH Zurich, Clausiusstrasse 25, 8092 Zurich, Switzerland.

*corresponding author

Tel: +61 434384664, Email: rosalindjcrossley@gmail.com

Running Title: Tracing HSEs through subduction

ABSTRACT

The highly siderophile elements (HSE) include the economically critical platinum group elements (PGE; Os, Ir, Ru, Rh, Pt, Pd, Au and Re), gold and rhenium. The HSE are redox sensitive in mantle and seafloor environments and have a strong affinity to iron and sulphur, therefore their distribution within the subducted mantle lithosphere record changes to oxidation state and sulphidation. The mobility of the HSE during subduction has important implications for Re–Os isotopic signatures in the mantle, and the formation of Cu-Au arc-related ore deposits.

In this study, subducted rock samples from Alpine Corsica are used to track the HSE in serpentinites and hybrid ultramafic/mafic rocks through the subduction cycle. A comparison of bulk rock HSE concentrations to those in pre-subduction analogues provides insights into the transfer of the HSE throughout the subduction cycle. Serpentinites subducted to blueschist-eclogite facies conditions have similar HSE concentrations to primitive upper mantle (PUM) concentrations, therefore it is concluded that the HSE are not mobilised from serpentinites on the scale of the whole rock or greater. Therefore, as suggested in previous studies, crustal lithologies may be more important contributors of the HSE to the sub-arc mantle, particularly Pt, Pd and Re. In contrast, HSE concentrations in hybrid rocks (talc schist and chlorite schist) deviate from protolith concentrations. Rhenium is higher in the talc schist, and Ir and Ru are lower in the chlorite schist than in the primitive upper mantle (PUM), or possible mafic protoliths.

Mineral parageneses place temporal constraints on the growth of hosts to the HSE (sulphides, oxides and metal alloys), and record changes to the activities of oxygen and sulphur (aO_2–aS_2), and hence redox conditions, from pre-subduction to exhumation. Laser

ablation-inductively couple plasma mass spectrometry (LA-ICP-MS) was used to determine the HSE concentrations in sulphides and oxides, and the detection of small (~2–25 μm^2) platinum group minerals utilised high resolution SEM mapping techniques. The prograde and retrograde sulphides have lower HSE concentrations compared to sulphides from pre-subduction settings. Therefore, the redistribution of the HSE on a mineral scale from sulphides to alloys and/or other sulphides has occurred within the serpentinites, which may reflect more reducing conditions during serpentinisation or subduction, consistent with the results of thermodynamic modelling. In contrast, the mineral assemblages in the hybrid rocks imply an increase in the extent of sulphidation and oxidation, and higher fluid:rock ratios during exhumation, coincident with Re enrichment in the talc schist, and a decrease in the concentrations of Ir and Ru in the chlorite schist, at length scales greater than those of the rock samples. Therefore, hybridisation of lithologies at the slab-mantle interface may enhance the transfer of the HSE to the sub-arc mantle. If Re transfer from the slab to the sub-arc mantle is possible, this questions the robustness of Re-Os isotope signatures as tracers of crustal recycling.

Key words: Highly siderophile elements; *in-situ*; redox; subduction; mantle;

INTRODUCTION

Subduction of redox sensitive elements can influence the oxidation state of the sub-arc mantle, deep mantle and metamorphic fluids released from the subducting slab (Evans 2012). The oxidation state of the sub-arc mantle is of particular significance because genetic models for arc-related Cu-Au deposits require an oxidised sub-arc mantle (e.g., Mungall 2002). The mineral hosts of the highly siderophile elements (HSE; platinum group elements (PGE), Re and Au) are redox sensitive, and include sulphides, spinels and PGE-rich alloys (e.g., Mitchell & Keays, 1981; Hart and Ravizza 1996; Puchtel and Humayun 2001; Pagé et al. 2012; Pagé and Barnes 2016; Brenan and Andrews 2001). *In-situ* analysis of the HSE hosts in rocks that have undergone subduction and subsequent exhumation can therefore provide insights on the cycling of the HSE, fluid composition and redox conditions. Textural analysis of mineral hosts to the HSE, combined with trace element chemistry, can be used to assess their stability during subduction metamorphism and exhumation, the release or retention of redox sensitive elements (Fe, S and PGE), and, therefore, the transfer of redox budget to the sub-arc mantle. Furthermore, the PGE and Au are economically critical elements, therefore understanding the behaviour of these elements during subduction is vital to the discovery of new arc-related ore deposits (e.g., McInnes et al. 1999; Richards 2009). In spite of these incentives, *in-situ* studies of the HSE hosts in subducted rocks are scarce, with notable exceptions (e.g., Aulbach et al. 2012; Dale et al. 2009; Evans et al. 2014).

Processes that affect HSE hosting lithologies (hydrated mantle lithosphere, altered oceanic crust, seafloor sediments and continental units from extended continental margins) during subduction can be difficult to distinguish because the hosts are affected by multiple stages of alteration; on the seafloor, and during subduction and exhumation. Through the measurement of HSE concentrations in sulphides, spinels, alloy phases and platinum group minerals (major hosts of the HSE), in combination with mineral textural analysis, redox conditions can be recorded because distribution of

the HSE is sensitive to the concentration of sulphur (e.g., Fleet et al., 1999), oxygen activity (aO_2) and sulphur activity (aS_2) (e.g., Mungall and Brenan 2014). For example, Re is incorporated into silicates and spinels under reducing conditions (Fonseca et al., 2007; Hart and Ravizza, 1996), and Pt alloys are considered to be stable under low aO_2 (Mungall and Brenan, 2014), and low aS_2 (Peregoedova et al., 2004, Barnes et al., 2012, and Baker 2004).

The mantle lithosphere can be exhumed on the seafloor at slow to ultra-slow spreading margins, where it is serpentinised via interaction with seawater. Upon subduction, the hydrated mantle lithosphere component of the slab dehydrates at depth within the subduction channel, where the dehydration of antigorite can release large volumes of fluids to the sub-arc mantle (e.g., Debret et al. 2014; Debret and Sverjensky 2017; Deschamps et al. 2013; Scambelluri et al. 2014; Scambelluri and Tonarini 2012). In addition, the nature of fluids released from serpentinites has important implications for element cycling. For example, elevated $^{187}Os/^{188}Os$ ratios in sub-arc mantle xenoliths from the Cascades, USA, and Japan, suggest ^{187}Os transport in slab-derived oxidised and Cl-rich fluids (Brandon et al. 1996). There are few previous studies of the transfer of the HSE from subducted lithologies, particularly from the mantle lithosphere component of the slab, with the exception of whole rock determination of HSE concentrations in serpentinites from La Corea mélange in Cuba (Blanco-Quintero et al. 2011), where the HSE were concluded to have behaved conservatively during metamorphism.

Mixing of lithologies, including sediments/oceanic crust and mantle lithosphere, along the slab/sub-arc mantle interface at high pressures produces ‘hybrid’ rocks, which have heterogeneous chemical and isotopic signatures (e.g., Spandler et al. 2008; Spandler and Pirard 2013). Hybrid rocks have been recognised as important carriers of volatile elements including sulphur, to greater depths than that of serpentinised mantle (Spandler et al. 2008; Spandler and Pirard 2013), therefore hybrid rocks could transport fluids and fluid mobile elements to the sub-arc mantle. Highly siderophile element concentrations in the rinds of eclogite facies blocks within subduction mélange from the

Franciscan Complex (USA) and the Samana Metamorphic Complex (Dominican Republic) were found to be similar to those in surrounding peridotites; one interpretation is that this records centimetre scale HSE mobility, although physical mixing is considered more likely (Penniston-Dorland et al. 2012). This uncertainty emphasises that redistribution of the HSE via interactions between lithologies during subduction requires further constraints. There are few studies of mineral-scale HSE transfer in subducted rocks, with notable exceptions. Dale et al. (2009) combined *in-situ* analyses of PGE in sulphides and whole rock analyses of gabbros unaffected by metamorphism, gabbroic eclogites and basaltic eclogites from the Zermatt-Saas zone, Western Alps, and concluded that Pt and Re in basalts, and Pd in gabbros were mobile on a rock sample scale or greater during metamorphism. Aulbach et al. (2012) used *in-situ* measurements of the HSE within sulphides in eclogitic diamonds from the Diavik mine, central Slave craton, to suggest that Au is mobilised by serpentinite-derived, reducing and Cl-poor fluids. Furthermore, it was inferred that Os, Ru and Pd can be transferred from the slab to the overlying mantle, based on the enrichment of these elements in sulphides from metasomatised garnet peridotites, representative of a depleted mantle protolith, from the Western Gneiss Region, Norway (Reilli et al., 2018).

In this study, we present the first *in-situ* trace element analysis of sulphides in subducted serpentinites and hybrid mafic/ultramafic rocks. Insights into subduction-modified HSE concentrations on the decimetre to millmetre scale are obtained through a comparison of whole rock and sulphide HSE concentrations in the studied samples to whole rock and sulphide HSE data from pre-subduction protoliths from the Kane Fracture Zone (KFZ), a slow-spreading centre (Alard et al. 2005; Luguet et al., 2003), and from the inferred ocean-continent transition (OCT) zone preserved in the Internal Ligurides (IL, Luguet et al. 2004). In addition, lithological controls on redistribution of the HSE are established through comparison with unmetamorphosed mafic rocks (Dale et al., 2009) and hybrid ultramafic/mafic rinds (Penniston-Dorland et al. 2012, 2014). Petrography and mineral composition data are used to construct mineral parageneses, with a focus on sulphides and oxides.

The results are integrated with sulphide HSE concentrations to provide insights into changes to redox conditions during sulphide and oxide formation and modification through the entire subduction cycle.

GEOLOGICAL SETTING

Alpine Corsica

Alpine Corsica consists of three main domains; the External Continental units, the Schistes Lustrés complex, and the uppermost units or the Nappes Supérieures (Vitale Brovarone et al. 2011, 2013). The External Continental units consist of deformed crystalline rock including continental basement rocks, such as the Tenda massif, and are inconsistently overlain by greenschist to blueschist facies sediments (Molli, Tribuzio and Marquer 2007; Tribuzio and Giacomini 2002; Vitale Brovarone et al. 2011). The Schistes Lustrés complex is considered to be comprised of several tectonometamorphic units, consisting of metaophiolites (including serpentinites, metagabbros and metabasalts), metasediments and slivers of internal continental slices (Vitale Brovarone et al., 2013). The uppermost units include the Balagne, Nebbio and Macinaggio nappe sheets (Vitale Brovarone et al., 2011; Meresse et al. 2012 and references therein).

The ophiolites and metasediments of the Schistes Lustrés complex, from which the samples in this study were collected, are considered to represent fragments of the ultra-slow to slow spreading Middle to Late Jurassic Piemonte-Ligurian oceanic basin and its cover sediments, which were subsequently subducted to high pressure-low temperature blueschist to lawsonite-eclogite facies from 55 Ma until 34 Ma (Magott, Fabbri, and Fournier 2016; Vitale Brovarone et al. 2013; Vitale Brovarone and Herwartz 2013). Retrograde metamorphism to greenschist facies occurred from the late Oligocene to early Miocene (Jolivet et al., 1990; 1991; 1998; Fournier et al., 1991, Magott et al., 2016).

The juxtaposition of the ophiolites and internal continental slices within the Schistes Lustrés complex is controversial. On the basis of small-scale structural work, deformation analysis and shear fabrics, some workers considered the units to have been juxtaposed as a result of tectonic thrusting of ophiolites onto continental basement during the Late Cretaceous as part of the Alpine Orogeny (e.g., Mattauer et al., 1981; Fournier et al., 1991). However, the juxtaposition could also have occurred during pre-Alpine Jurassic Tethyan extension in an ocean-continent transition (OCT) zone (Vitale Brovarone et al., 2011; 2013; Meresse et al., 2012), as proposed for other localities in the Western Alps (e.g., Beltrando et al., 2010). The evidence for an OCT setting is well-preserved in Alpine Corsica. For example, the pre-Alpine contact (a detachment fault) between ultramafic rocks and continental slices at Monte San Petrone, pre-dates high-pressure ductile fabrics, and the Jurassic-Cretaceous metasediments overlying the ultramafic rocks and continental slices do not show evidence of cataclastic deformation (Vitale Brovarone et al., 2011). Other evidence for an OCT setting is found within the Serra di Pigno region, where ultramafic clasts are found within carbonate metasediments, ophicalcites, and significantly variable metasedimentary successions interlayered with mafic and ultramafic lithologies and breccias are consistent with this interpretation (Meresse et al., 2012).

Serra di Pigno

Serra di Pigno is located ~10 km west of Bastia, on Cap Corse, Alpine Corsica, between Patrimonio in the west and Ville di Pietrabugno in the east (Meresse et al., 2012, Fig 1a–c). In this study, representative serpentinites proximal and distal to other lithologies were selected to assess lithological controls on the HSE distribution, in addition to the effects of the subduction cycle. The selected samples consist of serpentinites distal to other lithologies (CO13-31 and CO13-40, WGS 84, zone 32T, 0533430 mE 4729806 mN and 0533122 mE 4728302 mN) and serpentinites proximal to other lithologies (CO13-21, CO13-33 and CO13-55, 0533228 mE 4728387 mN, 0533514 mE

4729532 mN and 0533398 mE 4729368 mN, respectively, Fig. 1c). These samples are from the Patrimonio unit, which structurally overlies the Serra di Pigno gneiss and is below the Cima de Gratera metagabbro (Meresse et al., 2012).

Most of the Serra di Pigno region lies within the lawsonite-blueschist zone, based on *P-T* estimates of 1.3 GPa and 455 ± 35 °C (Lahondère and Guerrot, 1997). However, the eastern parts of the region are inferred to record eclogite facies peak conditions, based on Raman spectroscopy of carbonaceous material (Vitale Brovarone et al., 2013). According to the reclassified tectono-metamorphic units in Vitale Brovarone et al. (2013), our samples lie on or close to the boundary between the blueschist and eclogite terrains. This interpretation implies maximum peak metamorphism temperatures of 414–471 °C and pressures of 1.3–2.6 GPa (Lahondère and Guerrot, 1997; Vitale Brovarone et al., 2013).

Capu Corvoli

Samples of chlorite schist (CO14-03, WGS 84, zone 32T, 0529140 mE 4753069 mN), talc schist (CO14-04, 0529107 mE 4753071 mN) and metagabbro (CO14-05, WGS 84, zone 32T, 0529154 mE 4753091 mN) were collected from Capu Corvoli , Cap Corse, ~5 km north of the village of Pino (Fig. 1a, d). The samples are from a shear zone that lies parallel to a series of nearby thrust faults with WNW to NW-orientated fault planes (Fig. 1d), which have previously been interpreted to separate the lawsonite-blueschist Upper Castagniccia metasediments and lawsonite-eclogite ophiolites (Lahondère, 1992). These structures dip shallowly to the WNW to NW and the shear zone records top-to-the-west to NW shearing, consistent with thrusting of the hybrid samples and metagabbro over calc schist of the Upper Castagniccia unit. The top-to-the-west to northwest sense of shear is consistent with non-coaxial deformation associated with prograde metamorphism (Mattauer et al., 1977; 1981; Faure and Malavielle, 1981; Harris, 1985; Warburton, 1986; Magott et al., 2016).

Recent *P-T* estimates based on Raman spectroscopy on carbonaceous material (RSCM) suggest the Upper Castagniccia metasediments at Capu Corvoli record eclogite conditions (e.g., Vitale Brovarone et al., 2013 and references therein, Fig. 1a); maximum peak *P-T* estimates of the lawsonite-eclogite ophiolites are ~490–550 °C and 1.9–2.6 GPa (Ravna et al., 2010; Vitale Brovarone et al., 2013). Thus, the Capu Corvoli samples experienced higher pressure conditions than the Serra di Pigno samples.

METHODS

Sample collection

Thirty samples of serpentinites, metaquartzites, calc schists, metagabbros, metabasalts and hybrid talc schists and chlorite schists were collected from Serra di Pigno and Capu Corvoli. From those, a representative sub-set of samples was selected at Serra di Pigno to include serpentinites distal to metasediments, metagabbros and metabasalts (CO13-31 and CO13-55), and those adjacent to these lithologies (CO13-21, CO13-33 and CO13-55, Fig. 1b, d). The hybrid mafic/ultramafic samples from Capu Corvoli (CO14-03 and CO14-04) were taken from foliated slivers of altered dark green rocks with visible large pyrites (up to >1 cm), which were adjacent to metagabbro and in close proximity to calcareous schist (Fig. 1c, d).

Analytical Methods

Bulk composition Analysis

Approximately 55 g of representative, unweathered rock was crushed using a TEMA Tungsten Carbide mill. Measures for quality assessment and control included analysis of blank samples consisting of a quartz crush, sample duplicates (two crushes of the same sample), and sample replicates (separating a crushed sample into two sub-samples). Samples were analysed for major, minor and selected trace elements, including the HSE, C, S, FeO and total iron (as Fe_2O_3 in

Table 1), at Intertek Genalysis, Maddington, Western Australia. Major elements, Cr, Sc and V were analysed by lithium borate fusion followed by dissolution and inductively coupled plasma optical emission spectrometry (ICP-OES). ^{109}Ag, ^{75}As, ^{209}Bi, ^{114}Cd, ^{63}Cu, ^{115}In, ^{208}Pb, ^{121}Sb, ^{78}Se, ^{126}Te and ^{205}Tl were analysed by four acid (HF, HCl, HNO_3 and HClO) digestion and inductively coupled plasma mass spectrometry (ICP-MS). Dwell times were 0.1 to 1 second for ICP-MS analyses. Loss on ignition (LOI) was measured using Thermo Gravimetric Analysis at 1000ºC. The FeO content was determined via titration with ceric sulphate. Bulk sulphur and carbon concentrations were determined using an Eltra Infra-red carbon-sulphur (CS) analyser.

Whole rock PGE (Pt, Pd, Rh, Ru, Ir and Os) and Au were analysed with nickel sulphide fire-assay (NiS-FA) pre-concentration followed by ICP-MS. The method is described in detail in Gervilla et al., (2005) and is based on the method of Chan and Finch (2001). Twenty-five grams of the sample were fused with a flux of borax, soda ash, silica, nickel oxide and sulphur at 1200 ºC. The reaction with sulphur reduced NiO to NiS, and formed a NiS matte and an immicible slag, with PGE and Au sequestered in the matte. The NiS matte was separated from the slag, weighed, pulverised and dissolved in boiling HCl. PGE and Au were recovered as insoluble residues on a cellulose nitrate membrane filter. The PGE and Au were sealed in borosilicate test tubes and dissolved in aqua regia. Additive reagents enhanced the recovery of Os, which would otherwise have volatilised. The solutions were diluted with 10% nitric acid. Concentrations were determined using a Perkin Elmer Elan 9000 quadropole ICP-MS. Multiple mass numbers were measured including ^{99}Ru, ^{101}Ru, ^{105}Pd, and ^{108}Pd, and concentrations were derived from the ^{99}Ru and ^{108}Pd isotopes to minimise interference effects. Corrections were applied for ^{63}Cu and ^{61}Ni argide interferences, and for drift and plasma fluctuations.

The detection limits for the HSE are 1 ppb for PGE and 2 ppb for Au and Re. Two procedural blanks were measured as controls, where concentrations of the HSE are below detection limits, with the exception of Pd (1 ppb) and Re (2 ppb) in one measurement. Uncertainties in whole rock HSE are

reported in Electronic Appendix 1 (http://www.petrology.oxfordjournals.org). The use of NiS-FA for PGE analysis has been questioned; isotope dilution (ID) high-pressure Asher or Carius tube digestion techniques are considered to optimise PGE recovery and give low level blanks (e.g., Puchtel et al., 2004; Becker et al., 2006; Lorand et al., 2008). However, the results obtained in this study for the reference material AMIS0278 in this study are within 5% of certified concentrations (Electronic Appendix 1), therefore PGE recovery for our samples using the NiS-FA technique is considered to be acceptable. Two control blanks did not have detectable PGE, with the exception of Pd and Rh at the detection limit in one blank which was taken into consideration in the interpretation of results (Electronic Appendix 1). A benefit of the NiS-FA technique, for the purposes of this study, is that it involves the analysis of relatively large sample masses (25g of each sample was analysed in this study), in contrast to <5g typically used in isotope dilution techniques. The larger sample mass minimises nugget effects, which is particularly advantageous when platinum group minerals are present in the samples. Furthermore, Rh and Au can be analysed simultaneously using the NiS-FA technique (Savard et al., 2010).

Scanning Electron Microscopy

Thin section billets were cut perpendicular to foliation and parallel to lineation, and polished thin sections were made for optical microscopy, scanning electron microscopy (SEM) and energy dispersive spectroscopy (EDS). Samples for *in-situ* trace element analysis were selected after petrographic analysis using transmitted and reflected light microscopy and subsequent characterisation by SEM and EDS. Initial scanning electron microscopy and EDS were performed at the Microscopy and Microanalysis Facility (MMF), John de Laeter Centre (JdLC), Curtin University, using a Zeiss Neon 40EsB field emission SEM. All samples were coated with ~25 nm carbon prior to SEM and EDS work. The accelerating voltage for EDS was 20 kV. Small, opaque phases (1–5 μm) were detected and analysed using the Oxford Instruments Feature Mapping facility on the Tescan

Mira 3 SEM at the MMF. Copper was used to optimise and calibrate the detector. The BSE signal was used to set the thresholds for identification of metal alloys and sulphides; the lower threshold was set to a brightness slightly higher than that of magnetite. The running time for each analysis was ~5 to 12 hours per sample, depending on the number of features detected.

The results of feature mapping with the Tescan Mira 3 were complemented by analysis with the Tescan Integrated Mineral Analyser (TIMA) at the JdLC MMF, Curtin University. A bright-field search was employed, with a lower BSE threshold set to 90%. A 1 μm step size was used to optimise the detection of small grains. The counts per pixel were set to 3000. The analysis time was a total of ~5 hours in total for 9 thin sections. Data processing was carried out using the TIMA 1.4.4.1 software.

Electron Probe Microanalysis (EPMA)

Major and minor elements of carbon coated sulphides, oxides and silicates were quantitatively analysed on the JEOL 8530F Hyperprobe at the Centre for Microscopy, Characterisation and Analysis (CMCA), the University of Western Australia. Mean atomic number (MAN) background corrections were used throughout with an on-peak counting time of 20 seconds per element. The accelerating voltage was set at 15 kV, the beam current at 20 nA. Multiple analyses were carried out per grain to identify any sample heterogeneity. The standards used for calibration of sulphides were Ni, Co, Pyrite (Fe, S), Crocoite (Pb), ZnO, Cu, Bi_2Se_3, GaAs (As), and Sb. Data reduction was performed using the Probe for EPMA v.10.8.1 software package (Donovan et al., 2012). The compositions of the matrix silicate phases were necessary to correct LA-ICP-MS data for silicate contamination in sulphide grains <50 μm. The same conditions were used for analyses of silicates and oxides, however the standards were as follows; wollastonite (Si), rutile (Ti), Kakanui pyrope (Mg, Al), V, Cr_2O_3, magnetite (Fe for oxides), San Carlos olivine (Fe for silicates), Ni, Mn, Durango apatite (Ca), Jadeite (Na), orthoclase (K).

Laser Ablation - Inductively Coupled Plasma - Mass Spectrometry (LA-ICP-MS)

Trace element contents of sulphide and spinel grains were obtained *in-situ* by Laser Ablation Inductively Coupled Mass Spectroscopy (LA-ICP-MS) at the GeoHistory Facility, JdLC, Curtin University, using a Resonetics RESOlution M-50 with a Compex 102 Excimer laser, coupled to an Agilent 7700s quadropole ICP-MS. Prior to LA-ICP-MS, thin section billets were polished with 1 μm diamond paste. The background signal was collected for 20 s, followed by ablation of the sample grains for 40 s, at a repetition rate of 7 Hz for large grains and 10 Hz for smaller grains in order to obtain sufficient counts above limits of detection. Ablation was performed in an atmosphere of ultra-high purity He and N_2 with a laser energy density at the sample surface of 2 J/cm^2. The spot size was set to 70 μm for grains >70 μm in diameter and to 50 μm for smaller grains. The HSE laser ablation time-resolved spectrum were inspected to identify spikes in counts that indicated intersection of discrete HSE-bearing phases within the sulphide or spinel grains.

Data reduction was carried out using the IGOR Pro 6.36 platform and the Trace Elements data reduction scheme in Iolite v. 2.5 (Paton et al., 2011). The isotopes analysed include ^{101}Ru, ^{103}Rh, ^{105}Pd, ^{186}Re, ^{189}Os, ^{193}Ir, ^{195}Pt and ^{197}Au. Integration of the HSE in sulphides and spinels utilised Laflamme Po726 as the primary standard for PGE and ^{197}Au, and BonnSulphVI (a synthesised sulphide doped with HSEs; Bragagni et al., 2018) as the secondary standard for PGE and as the primary standard for Re. ^{57}Fe was used as the internal isotope standard for pentlandite, pyrite and spinel grains, due to the high concentration of Fe in these minerals and because ^{57}Fe is not subject to the ^{40}Ar ^{16}O interference on ^{56}Fe (Danyushevsky et al., 2011). However, for heazlewoodite, an Fe-poor sulphide, ^{34}S was used as the internal isotope standard.

The relative uncertainties on the HSE concentrations are ≤11%, with the exception of Pt where the relative deviation from accepted values was 25% (Electronic Appendix 2). The increased uncertainty for Pt could reflect heterogeneity in the standards at the 50 μm scale of analysis.

Potentially significant interferences include $^{63}Cu^{40}Ar$ on ^{103}Rh and $^{65}Cu^{40}Ar$ on ^{105}Pd, where ^{63}Cu is 69% of total Cu. However, Cu is present at relatively low concentrations in the sulphides (up to 2170 ppm) and spinels (up to 650 ppm) analysed. Where discrete Cu-rich phases were present within sulphide grains, the time resolved spectrum for each analysis was checked for correlations between the ^{65}Cu and ^{103}Rh and ^{105}Pd peaks (Electronic Appendix 3). A correlation between ^{65}Cu and ^{103}Rh and ^{105}Pd was observed in one grain, though other grains did not show a significant correlation, and ^{103}Rh was typically homogeneous throughout the ablation period, despite the heterogeneous Cu distribution. Therefore, interferences on Rh were deemed to have had a negligible effect on the calculated concentrations.

In addition, $^{61}Ni\ ^{40}Ar$ interferences on ^{101}Ru, may produce erroneously high concentrations of ^{101}Ru, however this effect is probably minimal because (1) ^{61}Ni is a low abundance isotope (1%), (2) there is no significant correlation between ^{101}Ru and ^{60}Ni (R^2=0.2) in the most Ni-rich sulphides (550000 ppm Ni), and (3) the concentrations of ^{101}Ru derived on Bonn SulphVI run as an unknown against Laflamme Po726 (where Bonn SulphVI contains 45600 ppm Ni) are in good agreement with the reference values. To quantify $^{61}Ni\ ^{40}Ar$ interferences on ^{101}Ru, apparent Ru concentrations in antigorite were measured (Electronic Appendix 5). The concentration of Ru in antigorite is assumed to be negligible, therefore the apparent Ru concentrations provide the $^{61}Ni\ ^{40}Ar$ production rate. A maximum of 0.06 ppm Ru was calculated for antigorite analyses with 5000 ppm Ni. At this production rate, and assuming that total Ni has 1.1% of the interference isotope ^{61}Ni, then 550,000 ppm Ni (the maximum concentration of Ni in pentlandite) would produce a systematic increase in calculated Ru concentrations of 0.07 ppm. For example, if Ru concentrations of sulphide grains are 4 ppm, then the contribution of the $^{61}Ni^{40}Ar$ production rate is 1.82% of the total, which is smaller than the uncertainty from other factors.

Analysis of small pentlandite grains (<50 μm) in serpentinites CO13-33 and CO13-55, necessitated inclusion of matrix antigorite in the ablation analysis volume, therefore analyses of HSE

concentrations in antigorite grains were necessary to correct trace element data. Transient ablation across sulphide grains would have been an appropriate method for ablation of small grains, but the shallower depth of ablation would have resulted in unacceptably low counts, and concentrations below detection for most HSEs. Instead, ^{28}Si was used as the internal standard for the reduction of matrix data because of its abundance in the NIST 612 standard, and because EPMA analyses revealed that the concentration of Si in the matrix are homogeneous (Electronic Appendix 4). The concentrations of S, Au, Re, Pd and Pt are negligible in the silicate minerals of the matrix (Electronic Appendix 5) and S concentrations within the analysed sulphide minerals are relatively homogeneous (Table 2, Electronic Appendix 6). Therefore, the S content of the sulphide analysis was used to calculate the proportion of matrix for each ablation, which was used to correct the content of PGE, Au and Re (Electronic Appendix 7).

Zoning of Cr and Fe in spinel grains was on a smaller length scale than the spot size, which produced mixed Cr and Fe peaks in the time resolved spectra. The maximum and minimum Fe concentrations for each grain were determined by EPMA (Electronic Appendix 8), and were used to calculate maximum and minimum HSE concentrations for each grain, using ^{57}Fe as the internal standard (Electronic Appendix 9).

PETROGRAPHY

The key features of the oxide and sulphide petrography are summarised below; full petrographic descriptions are provided in Electronic Appendix 10 and supplementary parageneses in Electronic Appendices 11 and 12. Further details of the sulphide petrography are outlined in Crossley et al. (2018). Modal abundance is provided as volume %. The abbreviations for the oxide and sulphide minerals are as follows: magnetite (mt), pentlandite (pn), pyrite (py) and pyrrhotite (po). Subscripts 0–3 after mt, pn, po and py assigns the phases to (0) primary or seafloor alteration (1) prograde metamorphism (2) the onset of exhumation, and (3) advanced stages of exhumation. The

Serra di Pigno serpentinite sample types that will be discussed in detail throughout the paper are abbreviated as follows; serpentinite samples distal to other lithologies (distal), serpentinite samples proximal to metagabbro and metaquartzite (proximal MGMQ), and serpentinite samples proximal to metagabbro and calc schist (proximal MGCS).

The sulphide and oxide parageneses (Fig. 3) were determined by cross-referencing with the silicate paragenesis, assuming that: fine-grained antigorite (atg1) grew during prograde metamorphism (Li et al., 2004); chlorite (chl1) grew during peak metamorphism (e.g., Padrón-Narvarta et al., 2013; Scambelluri et al., 2014; Evans and Powell, 2015); coarse, cross-cutting antigorite grew during early exhumation (atg2); and diopside (di2) grew during the onset of exhumation, based on di2 overprints of atg1 and chl1, and the similarity between the textural setting of the randomly orientated idioblastic prisms of di2 and other descriptions of retrogressive diopside (Groppo and Compagnoni, 2007).

Serpentinites: Serra di Pigno

Spinel All serpentinites from Serra di Pigno contain spinel (with a modal abundance of ~2–6%). These typically have Cr-Al cores and Fe-rich porous spinel and/or magnetite rims. Veins of magnetite are observed cross-cutting the Cr-spinel core. Concentric alternating Cr and Fe-rich bands are observed within large spinel grains (1–2.5 mm).

The Cr-Al spinel cores are inferred to have formed in the mantle prior to serpentinisation. Porous Cr-spinel cores, where fine-grained antigorite grains fill the pore space, are found in all serpentinite samples except CO13-31 (distal, Fig. 2a). This texture is consistent with alteration of primary spinel during seafloor serpentinisation and possible further alteration during prograde metamorphism (Evans and Frost, 1975; Bliss and MacLean, 1975; Wylie et al., 1987; Kimball, 1990; Frost 1991; Barnes, 2000; Mellini et al., 2005; Barra et al., 2014; Merlini et al., 2009; Mukherjee et al., 2010; Grieco and Merlini, 2012; Gervilla et al., 2012; Colás et al., 2014).

Magnetite rims on the Cr-spinel grains are overprinted by chl1 and/or fine-grained orientated and foliated matrix atg1 (Fig. 2a, b). Such magnetite grains also occur as rims on bastite mesh textures assigned to seafloor serpentinisation after pyroxene, and therefore these grains postdate early serpentine phases. In addition, magnetite contains inclusions of prograde atg1. Chlorite rims on magnetite further constrain this generation of magnetite to growth during or prior to prograde to peak metamorphism, and therefore these magnetite grains are referred to as magnetite1 (mt1).

A later generation of magnetite (mt2, ~3–8%) replaces fine-grained matrix antigorite, is included in or synchronous with later generations of cross-cutting coarse atg2. Further supporting evidence for the late-stage growth of this magnetite includes the network and brecciated texture in the serpentinite sample CO13-21 (proximal MGMQ), which is consistent with fluid infiltration under brittle conditions, such as those expected during retrogression.

Sulphides Primary sulphides, identified as polyhedral blebs with concave inward grain boundaries (e.g., Seyler et al., 2007), were not observed in the samples. The earliest sulphide phases include chalcopyrite associated with Cu-Fe±Ni alloys within porous Cr-spinel. Pentlandite1 (typically 1–3% in modal abundance) consists of medium (up to 50 μm) to fine-grains (1–5 μm), is associated with mt1 and overprints the foliation defined by fine-grained antigorite (atg1), with inclusions of atg1 incorporated in pn1 (Fig. 2c). Feature mapping revealed the presence of trace Co-rich pn1 (>10 wt% Co) within antigorite veins in serpentinite sample CO13-33 (proximal MGMQ). The inclusion of atg1 in pn1, and the replacement of pn1 rims by a later generation of antigorite (atg2), restrict pn1 growth to a stage prior to retrogression (Fig. 3a).

Grains of py1 (<5 μm, <1%) in serpentinite sample CO13-55 (proximal MGMC), occur as rims on, and are in textural equilibrium with mt1 (Fig. 2a). In addition, this generation of pyrite along with chalcopyrite is included in atg2 and di2, silicate phases attributed to the onset of exhumation. The growth of py1 is therefore attributed to prograde metamorphism (Fig. 3a).

Heazlewoodite is the predominant sulphide phase in the serpentinite sample CO13-31 (distal). Grains of hz1 are ~50–100 μm in diameter, include grains of atg1, and are associated with or are cross-cut by atg2 and, in places, balangeroite veins (Fig 2d, e). In addition, hz1 co-exists with or contains inclusions of early euhedral magnetite (mt1, Fig 2e) and millerite (Fig. 2f). Millerite contains inclusions of prograde antigorite (atg1, Fig 2f). It is possible that the antigorite inclusions are recrystallised early lizardite, therefore millerite growth could have occurred during seafloor serpentinisation. Hz1 and Pn1 (including the Co-rich variety), are assigned to prograde to peak metamorphism (Fig. 3a), based on their association with prograde to peak phases; chlorite, balengeroite and antigorite.

Grains of pn2 (~10–50 μm) contain inclusions of fine-grained antigorite, overprints the foliation defined by fine-grained antigorite, and is overprinted by coarse laths of antigorite at the rim (Fig 2g, h). Pentlandite2 replaces the zoned Cr to Fe-rich spinels and chlorite (Fig. 2h), and contains inclusions of small Cr-spinel grains (2–3 μm). Additionally, pn2 replaces fine-grained antigorite associated with prograde deformation. In the case of serpentinite sample CO13-55 (proximal MGMQ), pn2 is associated with or replaced by di2 (10–30 μm, Fig. 2i). Pentlandite2 also occurs as rims on the edges of hz1 and/or pn1 grains or as euhedral grains in the matrix ~35–50 μm in size (Fig. 2g), is associated with or overprints late antigorite veins (Fig. 2h, i), contains inclusions of early fine-grained antigorite and is associated with or overprinted by a late generation of magnetite. The growth of pn2 is attributed to peak metamorphism through to early exhumation (Fig. 3a) because pn2 replaces chlorite and/or coarse antigorite (atg2, Fig. 2h), contains inclusions of fine prograde antigorite, and is synchronous with mt2 (Fig. 2g).

Grains of pn3 are euhedral to subhedral, texturally synchronous with, or occur as rims on, late antigorite cross-cutting veins (atg2, Fig. 2j) and mt2. Veins of atg2 replace prograde to peak phases including cpy1, py1, pn1 and mt1, in addition to phases associated with early exhumation, pn2 and mt2, thus pn3 is related to advanced stages of exhumation (Fig. 3a).

Alloys Mapping with SEM revealed trace 2–5 μm Pt-rich metal alloys on the rim of two heazlewoodite grains in CO13-31 (distal, Fig. 2k), 1–5 μm Fe-Cu±Ni alloys included within porous Cr-spinel grains in CO13-40 (distal) and 5 μm kamacite ($Fe_{0.9–0.95}Ni_{0.05–0.1}$) grains within 1–2 μm veins of balangeroite in CO13-33 (proximal MGMQ). The Cu-Fe±Ni alloys and chalcopyrite are replaced by antigorite and included in Cr-spinel, therefore these alloys are assigned to initial serpentinisation, formed in response to desulphurisation of chalcopyrite in highly reducing conditions associated with initial serpentinisation (e.g., Schwarzenbach et al., 2014). The Pt-rich alloys at the rim of hz1 grains are considered to have formed during subduction (Fig. 3a) because these replace hz1 at the rim and are replaced by chl1.

Hybrid rocks: *Capu Corvoli.*

Spinels The talc schist sample, CO14-04, contains spinel with Cr-rich cores (~2%) and Fe-rich magnetite rims (~3%, ~40–100 μm, Fig. 2l). Magnetite texturally postdates Cr-spinel and is cut by chl1, therefore growth occurred prior to peak metamorphism (Fig. 3b, Electronic Appendix 12).

The chlorite schist sample, CO14-03 contains large 1–5mm euhedral magnetite grains (Fig. 2n, 15%) which cross-cut the matrix comprised of orientated chl1 laths and fine atg1 intergrowths. The magnetite is replaced by titanate grains up to ~50 μm within the matrix (Fig. 2n). Titanite is considered to be a low-pressure phase (e.g., Laird & Albee, 1981; Spear, 1981; Ernst & Liu, 1998). Therefore, magnetite growth is assigned to the onset of exhumation (mt2) because it cuts the foliated chl1 and atg1 matrix, and predates the late titanite (Fig. 3b, Electronic Appendix 12).

Sulphides Pyrite is the dominant sulphide in both hybrid samples. In the talc schist sample, CO14-04, there are two texturally distinct forms of pyrite (py1 and py2). Grains of euhedral to subhedral py1 (5%) ~100 μm, contain inclusions of Cr-rich spinel (~5 μm) and pyrrhotite (po0, ~1–2 μm, Fig. 2l), and commonly show an iron hydroxide rim that includes ~5–10 μm pyrrhotite (po1, Fig. 2l). Inclusions of primary or seafloor phases in py1, and the observation that py1 and po1 cuts

the foliation defined by the talc matrix (talc1), suggests that py1 and po1 grew late during, or after, prograde metamorphism. The iron hydroxide rim that replaces the py1 and po1 most likely results from low temperature alteration at the most advanced stages of exhumation, as invoked previously for high pressure serpentinite samples from the Western Alps (Alpine Corsica and the Piedmont zone), the Greater Antilles, and the Himalayas (Malvoisin et al., 2017).

Euhedral grains of py2 (10%, 50–300 μm, Fig. 2m) overgrow the matrix of chlorite and talc1, and display intragranular fractures associated with brittle deformation. Pyrite2 is replaced by coarse talc at the rim (Fig. 2m) and contains inclusions of talc that are up to 50 μm in diameter, though these are connected to the matrix. Coarse talc grains (talc2) cut the talc1 and chl1 matrix, and are considered to record post-peak metamorphism and decompression associated with exhumation (Evans and Powell, 2015). Pyrite2 growth is assigned to the early stage of exhumation, based on the observations that py2 overgrows the talc1-chl1 matrix and precedes coarse talc grains (talc2, Fig. 3b, Electronic Appendix 12).

Euhedral aggregates of py3 occur on the rims of large magnetite grains (~3%, Fig. 2m), associated with fractures in magnetite. In CO14-03, py3 exists as euhedral aggregates (~50–100 μm) on the rims of large magnetite grains and within mt2 (<1%). Matrix py3 also occur as euhedral to subhedral single grains or aggregates (30–1000 μm, ~2%). Pyrite3 grew during a late stage of exhumation after magnetite, based on its presence as rims on, or in fractures within large euhedral magnetite grains (Fig. 2m, Fig. 3b, Electronic Appendix 12).

Alloys Pt-rich alloys (10 μm^2, Fig. 2o) and Cr-Al spinel are found near the rim of py1 in the talc schist (CO14-04). The Cr-Al spinel is likely to have crystallised in the mantle prior to serpentinisation, although it may have also undergone alteration on the seafloor. Based on the spatial proximity to the Cr-Al spinel, Pt-rich grains are considered to be primary or associated with seafloor alteration (Fig. 3b, Electronic Appendix 12).

RESULTS

Whole rock major element data

Serpentinites: Serra di Pigno

Major and trace element data for the Serra di Pigno serpentinites (CO13-31, CO13-40, CO13-21, CO13-33 and CO13-55) are reported in Table 1. Loss on ignition (LOI) provides a proxy for the extent of serpentinisation when serpentine is the dominant hydrous phase; pure serpentine contains ~13 wt% H_2O (Deer, Howie and Zussman, 1962). The LOI values of 10.7–12.1 wt% for the Serra di Pigno serpentinites are similar to the average LOI of 11.2 wt% calculated from a compilation of subducted serpentinites (Deschamps et al., 2013). The Al_2O_3 contents range from 1.19–2.01 wt%, and have low concentrations of CaO, (0.03–0.16 wt%), with the exception of CO13-55 (proximal MGCS), which contains 2.04 wt% CaO. The MgO contents range from 36.4–39 wt%. Nickel and Cr concentrations range from 2028–2287 ppm and 1812–2750 ppm, respectively. All the serpentinites have similarly low C contents with a range from 200–300 ppm.

Sulphur concentrations are generally low and variable, with concentrations of between 200-1100 ppm. Serpentinite samples CO13-21 and CO13-33 (proximal MGMQ) contain the highest concentrations. The total iron content, reported as $Fe_2O_{3\ tot}$, is 6.42–9.09 wt%. The concentration of Fe_2O_3 is 2.80–5.76 wt%, with the lowest concentration in CO13-55 and the highest in CO13-33.

Hybrid rocks: Capu Corvoli

The Capu Corvoli hybrid rocks CO14-03 and CO14-04 have lower LOI values than Serra di Pigno (7.24 wt% and 5.45 wt%, respectively). These values are consistent with the low proportion of serpentine, the high proportion of anhydrous minerals, particularly magnetite, in CO14-03, and with the high mode of talc in CO14-04; talc has a water content of only ~4.6 wt%.

Compared to the Serra di Pigno serpentinites, the chlorite schist sample, CO14-03, has a higher concentration of ΣFe_2O_3 (20.4 wt%) and Al_2O_3 (10.9 wt%), and a lower concentration of SiO_2 (34.4 wt%). The CaO content of CO14-03 is similar to the Serra di Pigno serpentinites. The high Fe concentration is consistent with the high magnetite mode, and the high Al_2O_3 content is consistent with the high chlorite mode. In contrast, the talc schist sample, CO14-04, has similar Al and Fe concentrations to the Serra di Pigno samples with 1.82 wt% Al_2O_3 and 8.5 wt% ΣFe_2O_3, but the MgO and SiO_2 concentrations are different at 24.8 wt% and 58.7 wt%, respectively. These features of the whole rock composition reflect the high modal abundance of talc. The CaO content of CO14-04 is 4.97 wt%, which is higher than that of the serpentinites and may record some degree of rodingitisation prior to subduction (e.g., Li et al., 2008; Panseri et al., 2008).

The Cr and Ni concentrations of CO14-03 are 621 ppm and 613 ppm, respectively. These values are lower than values for the primitive and depleted mantle values, and are consistent with a mafic component in the protolith (e.g., Spandler et al., 2008). In contrast, the Cr and Ni concentrations in the talc schist sample, CO14-04, are similar to the Serra di Pigno serpentinites and to typical mantle concentrations with 2061 ppm Cr and 1579 ppm Ni.

The Capu Corvoli hybrid rocks contain higher sulphur concentrations than the Serra di Pigno serpentinites, with 540 ppm S in CO14-03, and 960 ppm S in CO14-04. The high S concentration is consistent with the higher mode of sulphides in these samples, and with sulphur-rich pyrite as the dominant sulphide rather than pentlandite and heazlewoodite, which are S-poor in comparison to pyrite.

The metagabbro proximal to the hybrid samples (CO14-05, Table 1) contains 46.5 wt% SiO_2, 13.7 wt% Al_2O_3, 7.45 wt% MgO, 12.3 wt% $\sum Fe_2O_3$ and 2.78 wt% TiO_2. The S content is 670 ppm, which is close to the average sulphur concentrations of CO14-03 and CO14-04 (Table 1).

Sulphide major element data

Major element concentrations were measured with EPMA for the sulphides analysed by LA-ICP-MS (Table 2, Fig. 4). Feature mapping revealed pyrrhotite, millerite and chalcopyrite grains that were too small for LA-ICP-MS analysis (<5 μm, Fig. 3). The formulae of the sulphide minerals were calculated, assuming usng charge balance and using stoichiometric constraints. All sulphides were close to stoichiometric, including millerite (NiS) in CO13-21 (proximal MGMQ) and CO13-31 (distal), pyrite (FeS_2) and chalcopyrite ($CuFeS_2$) in CO13-55 (proximal MGMC), and pyrrhotite ($Fe_{7.1}S_{8.0}$) in CO14-04 (talc schist). The average composition of pentlandite is $Fe_{3.6}Ni_{4.9}Co_{0.3}S_{8.1}$ in CO13-33 (n=37) and $Fe_{3.7}Ni_5Co_{0.3}S_{8.1}$ in CO13-55 (n=33). There is a small amount of Fe substitution for Ni in heazlewoodite in CO13-31 (up to 0.01 Fe per formula unit of Ni_3S_2). Minor Co and Ni replace Fe in pyrite (up to 0.01 cations per formula unit) in CO14-03 and CO14-04 (Electronic Appendix 6).

Whole rock highly siderophile elements

Serpentinites: Serra di Pigno

Whole rock HSE data for the Serra di Pigno serpentinites were normalised to primitive upper mantle (PUM; Becker et al., 2006; Fischer-Gödde et al., 2011; Fig. 5a, Table 1), and compared to subducted serpentinites from La Corea, Cuba (Blanco-Quintero et al., 2011), serpentinised peridotite from the Internal Ligurides (IL), which represents pre-subduction Tethyan lithosphere from an OCT or slow-spreading centre setting (Luguet et al., 2004) and serpentinised peridotites from the slow-spreading Kane Fracture Zone (KFZ; Luguet et al., 2003; Alard et al*.,* 2005, Fig. 5a).

Osmium concentrations vary from 2 ppb in CO13-55 (proximal MGCS) to 4 ppb in CO13-31 (distal). Iridium and Ru concentrations are similar in all serpentinite samples (3–4 ppb Ir and 5–6 ppb

Ru), similar to concentrations reported for PUM and pre-subduction analogues from the IL and KFZ (Luguet et al., 2004; Luguet et al., 2003; Alard et al., 2005).

The Rh concentration in all samples is ~1 ppb, which is close to the detection limit, and similar to the concentration of Rh in the PUM. Platinum concentrations in the samples are all similar and indistinguishable the Pt contents of the PUM and KFZ peridotite (6–9 ppb). Palladium concentrations in the Serra di Pigno (6–11 ppb) serpentinites are consistent with Pd in serpentinites from the IL, where concentrations of up to 12 ppb are reported (Luguet et al., 2004), and KFZ peridotites which contain up to ~8 ppb Pd (Luguet et al., 2003; Alard et al., 2005).

The Serra di Pigno serpentinites do not contain detectable Re or Au, with the exception of the CO13-31 (distal), which contains 4 ppb Au.

Hybrid rocks: Capu Corvoli

Normalised whole rock data for the hybrid rocks were compared to data from the Zermatt-Saas gabbros and gabbro eclogites, similar in composition to the mafic end member of the hybrid rock (Dale et al., 2009), mantle protoliths (Luguet et al., 2003, 2004; Alard et al., 2005), and hybrid mafic/ultramafic rinds (Penniston-Dorland et al., 2012, Fig. 5a)

The Capu Corvoli hybrid rocks have similar concentrations of Os to the Serra di Pigno serpentinite samples (3–5 ppb). The talc schist sample (CO14-04) has similar concentrations of Ir (4 ppb) and Ru (5 ppb) to the Serra di Pigno serpentinite samples, whereas the chlorite schist sample (CO14-03) contains <1 ppb Ir and 2 ppb Ru. The lower concentrations of Ir and Ru in CO14-03, are consistent with concentrations previously reported for hybrid rinds (Penniston-Dorland et al., 2012).

Only the talc schist sample, CO14-04, contains Rh significantly in excess of the detection limit (2 ppb). The chlorite schist sample, CO14-03, has a Pt content approximating that of hybrid mafic/ultramafic rinds studied previously (Penniston-Dorland et al., 2012; 2014) and peridotite from

the IL (Luguet et al., 2004). The Capu Corvoli hybrid rocks have similar Pd concentrations (8 ppb) to the Serra di Pigno serpentinites, and to peridotites from the IL and KFZ (Luguet et al., 2003; Alard et al., 2005).

The talc schist sample (CO14-04) has a Re concentration significantly in excess of the concentration measured for the highest blank (6 ppb), whereas the chlorite schist sample (CO14-03) has the same concentration as the blank at 2 ppb (Fig. 5a). Rhenium is therefore higher in concentration in the hybrid rocks compared to the Serra di Pigno serpentinites. Gold concentrations in both samples are 4–5 ppb.

Sulphide highly siderophile elements

Ni-rich sulphides

In-situ LA-ICP-MS derived HSE data for sulphides are of sufficient grain size for analysis (hz1 in CO13-31; distal, pn2 in CO13-33; proximal MGMQ, and pn3 in CO13-55; proximal MGCS) are reported in Table 3. The Serra di Pigno sulphide HSE concentrations are compared to assumed pre-subduction concentrations, using pyrrhotite and pentlandite HSE data from the KFZ (Alard et al., 2005), pentlandite and pyrrhotite data from the Internal Ligurides, Ligurian Alps (Luguet et al., 2004). Additionally, pyrrhotite/pyrite data from Zermatt-Saas gabbro (Dale et al., 2009) and Zermatt-Saas gabbro eclogite pyrite data from the Zermatt-Saas (Dale et al., 2009) are compared to the Serra di Pigno sulphide data to assess any changes in concentration associated with proximity to other lithologies.

Iridium-group PGE concentrations in heazlewoodite and pentlandite in the Serra di Pigno serpentinites, CO13-31 (distal), CO13-33 (proximal MGQS) and CO13-55 (proximal MGCS), are in the order of $Ir \leq Os < Ru$. Ruthenium concentrations are similar to those recorded in sulphides from the KFZ (Luguet et al., 2003; Alard et al., 2005), with higher concentrations in heazlewoodite than

pentlandite, with the exception of grain s4-3 in CO13-55. In comparison, Os and Ir concentrations are more variable. The concentrations of Os and Ir in two grains (CO13-31 s1 and CO13-55 s4-3) are similar to those in the KFZ sulphides, but the Os and Ir in most of the heazlewoodite grains are more similar to hydrothermal sulphides from the IL (Luguet et al., 2004). The concentration of Os and Ir in pentlandite are lower than those in heazlewoodite, and are similar to those recorded in sulphides from Western Alpine gabbros (Dale et al., 2009).

Concentrations of the PPGE are variable in pentlandite and heazlewoodite in the Serra di Pigno serpentinites, with Pt < Pd ≤ Rh. The Rh and Pd concentrations in pn2 grains from CO13-33 (proximal to metagabbro and metaquartzite) are up to 100 times those in heazlewoodite and pn3 grains in CO13-55 (proximal to metagabbro and calc schist).

Rhenium is below detection in all sulphides within Serra di Pigno serpentinites, and Au is below detection in most sulphide grains, with the exception of two hz1 grains in CO13-31 (distal), which contain 0.044 and 0.049 ppm Au, and one grain of pn3 in CO13-55 (proximal MGCS) with 0.191 ppm Au.

Pyrites

Grains of py2 and py3 in the Capu Corvoli hybrid rocks, CO14-03 and CO14-04, are depleted in the IPGE relative to heazlewoodite and pentlandite in the Serra di Pigno serpentinites. The concentrations of Os and Ir are at or below the detection limit, while Ru concentrations are up to 30 ppb in py2 in the talc schist sample, CO14-04, and below the detection limit in py3 grains within the chlorite schist, CO14-03. These concentrations are consistent with those reported for pyrites from eclogite-facies Alpine metagabbros (Dale et al., 2009).

Trends of PPGE concentrations in pyrites from the Capu Corvoli hybrid rocks are similar to trends shown by Serra di Pigno serpentinites with Pt < Pd ≤ Rh. However, the absolute

concentrations of the PPGE are lower than those in the Serra di Pigno serpentinites by up to an order of magnitude. Palladium is slightly lower in concentration than Rh, and Pt approximates or is less than detection limit.

Concentrations of Re in pyrite from the Capu Corvoli hybrid samples are higher than Re concentrations in the Serra di Pigno Ni-rich sulphides. For example, the concentration of Re in py2 grains in the talc schist sample, CO14-04, is up to 1000 times higher than concentrations in the Serra di Pigno sulphides, and is similar to Re concentrations reported in KFZ sulphides (Luguet et al., 2003; Alard et al., 2005). The concentrations of Re increases from core to rim in py2 grains in the talc schist sample CO14-04. In comparison, py3 grains in the chlorite schist sample, CO14-03, have Re concentrations that vary from below detection to two orders of magnitude less than those in the CO14-04 py2 grains. Gold concentrations are low or below the detection limit in py2 grains from CO14-04. In contrast, Au is detectable in py3 from CO14-03 grains (0.003–0.086 ppm Au).

Spinel highly siderophile elements

The concentrations of the IPGE in most spinel grains are below the limits of detection. Detectable concentrations of Os and Ir were found in only one grain in the serpentinite sample CO13-31 (distal; 0.723 ppm maximum); in this grain the IPGE are ranked in order of highest concentration as Ir < Os < Ru. Ruthenium was above detection limits in this grain, and another two grains in CO13-31 (Ru ≤ 1.19 ppm), and in six spinel grains in serpentinite sample proximal to metaquartzite and metagabbro (CO13-33, 0.0049–0.476 ppm).

Rhodium (≤ 0.140 ppm), Pt (≤ 0.062 ppm) and Pd (≤ 0.249 ppm) concentrations are above the limits of detection in one spinel grain in CO13-31 (distal). Rhodium concentrations are above the detection limit in three grains from (≤ 0.009–0.049 ppm). Platinum concentrations are below the limits of detection in all grains analysed, and Pd was only above the limits of detection in one spinel grain in CO13-33 (≤ 0.025 ppm).

DISCUSSION

To trace the HSEs through the subduction cycle, the geodynamic setting and composition of the likely protoliths, the whole-rock content and mineral hosts of HSEs in the protoliths to the serpentinites and the hybrid rocks are discussed. The stability of the mineral phases that host the HSEs are considered, which are sensitive to aO_2 and aS_2 (e.g., Evans et al., 2017) and the oxide–sulphide assemblages are used to determine whether aO_2 and aS_2 were internally or externally buffered. Insights on the likely behaviour of the HSEs within the subduction zone, as a result of changes in redox conditions and/or fluid infiltration at depth on various scales, are obtained through comparison of the measured contents in the Serra di Pigno and Capu Corvoli whole rock and sulphide samples to pre-subduction protoliths.

Geodynamic setting of the protoliths

Several field observations, including continental slices adjacent to ultramafic rocks, clasts of ultramafic rocks included in carbonaceous sediments, the presence of ophicalcites, and the interlayering of sediments with mafic and ultramafic lithologies at Serra di Pigno and other localities within Alpine Corsica, are consistent with a pre-subduction OCT setting (e.g., Vitale Brovarone et al., 2011; 2013; Meresse et al., 2012; see Geological Setting). The KFZ (a slow-spreading centre) and the IL (an ultra-slow spreading centre or OCT setting) provide analogues for the possible pre-subduction setting of the serpentinite samples studied here. Serpentinites from such seafloor settings have depleted mantle protoliths (e.g., Deschamps et al., 2013).

The Serra di Pigno samples were likely serpentinised in an oceanic setting prior to subduction based on the CaO contents, which are lower than those of depleted mantle (Salters and Stracke, 2004); values of CaO/Al_2O_3 range from 0.03–0.10, in contrast to the depleted mantle value of 0.82. The value of CaO/Al_2O_3 for CO13-55 is higher, at 1.21, and likely records metasomatic effects related to the close proximity of this sample to calc-schist.

The hybrid nature of the Capu Corvoli samples originated either via hydrothermal fluid metasomatism, or via mechanical mixing either on the seafloor or during subduction prior to peak metamorphism (Fitzherbert et al., 2004; Spandler et al., 2008). Given that the composition of the Capu Corvoli rocks do not reflect a composition between the two end members of serpentinite and metagabbro (Table 1), it is proposed that the composition of these rocks are a result of metasomatic alteration.

Whole rock HSE contents of protoliths to the serpentinites

Melting depletes Re > Au > Pd > Pt > Rh progressively in the residual mantle (Pearson et al., 2004; Becker et al., 2006; Fischer-Gödde et al., 2011). The IPGE are highly compatible, therefore their concentrations are considered to increase with melting. The PPGE are less compatible and partition into melts, especially sulphide-bearing melts (e.g., Barnes et al., 1985). Therefore, the samples with the most depleted protoliths should have the lowest PPGE, Au, and Re contents and the highest IPGE contents. The residual mantle becomes progressively depleted in minerals that host the HSEs, such as sulphides, as the degree of melting increases (e.g., Fischer-Gödde et al., 2011). In the ultra-slow to slow spreading setting of the samples studied, the low degree of melting would likely be insufficient to extract sulphide melt completely from the mantle residue, hence Pt and Pd would not be highly depleted (e.g., Barnes et al., 2015).

Whole-rock HSE concentrations in the Corsican serpentinites were compared to those of depleted mantle, primitive upper mantle (PUM), serpentinites from the KFZ, and the IL. The bulk rock HSE concentrations of the Serra di Pigno samples are similar to those estimated for PUM (Becker et al., 2006; Fischer-Gödde et al., 2010), except for Pd, which is elevated relative to PUM in CO13-31 (distal).

The Pd and Pt concentrations of the Serra di Pigno serpentinites are similar to those of the KFZ and IL seafloor analogues, where higher concentrations of Pd and Pt relative to depleted mantle

are considered to result from a combination of melt percolation in the oceanic mantle and low to moderate degrees of partial melting (Luguet et al., 2003; 2004; Alard et al., 2005). Therefore, it is possible that primary magmatic processes caused the Pd and Pt enrichments in the Serra di Pigno samples. Melt percolation might also have modified the other HSE concentrations to similar values to the PUM. If this was the case, there is no need to invoke modification of the whole rock concentrations of these elements by subduction to blueschist–eclogite facies metamorphism and subsequent exhumation.

Whole-rock HSE contents of protoliths to hybrid rocks

The mineralogy, bulk composition, textures, and field relationships of the Capu Corvoli hybrid rock samples, CO14-03 and CO14-04, are consistent with those of ultramafic/mafic rocks previously described as 'hybrid' rocks in mélange zones (e.g., Spandler et al., 2008; Miller et al., 2009; Barnes et al., 2014), and are similar in composition to high-pressure chlorite and talc-schists from New Caledonia (Spandler et al., 2008) associated with hybridisation either by hydrothermal fluid metasomatism or mechanical mixing, which may have occurred on the seafloor or during subduction (Fitzherbert et al., 2004; Spandler et al., 2008). The deformation and sense of shear of the metagabbro and serpentinite observed in the field is consistent with deformation during prograde metamorphism (see Geological Setting).

The chlorite schist has low SiO_2, high MgO, FeO and Al_2O_3. The talc schist has high SiO_2, and low LOI (Table 1). The compositions of the Capu Corvoli rocks are not a simple mix between serpentinite and metagabbro end-members (Table 1), which indicates that these hybrid rocks most likely formed by fluid alteration of peridotites or gabbroic protoliths.

The HSE concentrations of the Capu Corvoli samples, except for Ir and Ru in CO14-03, are higher than HSE concentrations reported for hybrid and mafic samples elswhere (Dale et al., 2009; Penniston-Dorland et al., 2014), but are similar to the HSE concentrations of serpentinites from the

KFZ (Luguet et al., 2003; Alard et al., 2005) and IL (Luguet et al., 2004). In particular, the Re concentration of the talc schist exceeds that of the Serra di Pigno serpentinites and their protoliths. The low concentrations of Ir and Ru in the chlorite schist sample, CO14-03, compared to those in pre-subduction peridotite protoliths, are consistent with reports of hybrid rocks elsewhere (Penniston-Doland et al., 2012; 2014). In these cases, it has been proposed that low HSE concentrations were part of the samples' mafic heritage.

The similarity between the concentrations of most of the HSE in the hybrid rocks and in their inferred pre-subduction ultramafic protoliths in the KFZ and IL implies that changes to whole-rock scale distribution of the HSE during metasomatism and hybridisation are not required to explain most of the measured values. However, explanations are required for the apparent decoupling between Ir–Ru and Os in the chlorite schist (CO14-03) and the high Re concentrations in the talc schist (CO14-04); possible mechanisms are discussed below.

Mineral hosts of the HSE in the serpentinites

Background

Experiments suggest that the HSEs are usually chalcophile and partition into sulphide phases (e.g., Patten et al., 2013; Peach et al., 1990; Peach et al., 1994; Roy-Barman et al., 1998; Andrews and Brenan, 2002; Gannoun et al., 2004, 2007; Mungall and Brenan, 2014). However, there are exceptions. Rhenium can behave as a lithophile element at high oxygen activities (e.g., Fonseca et al., 2007; Mallmann and O'Neill, 2007), and can be compatible in silicate and oxide phases including pyroxene, olivine, garnet and spinel (Hart and Ravizza, 1996; Mallmann and O'Neill, 2007; Righter and Hauri, 1998; Burton et al., 1999, 2000, 2002). Osmium, Ir and Ru are compatible in Cr-bearing spinel, Pt and Pd are moderately compatible (Hart and Ravizza, 1996; Puchtel and Humayun, 2001), and Ru, Rh, and Ir are highly compatible in Fe^{2+}-bearing spinels under moderate to highly oxidising conditions (Capobianco and Drake, 1990; Capobianco et al., 1994, Righter et al., 2004). The

compatibility of Ir, Rh, Pt, and Pd increase in Fe-rich spinels with decreasing Fe^{3+} (Brenan et al., 2012).

The chalcophile nature of the HSE means that sulphides are the main control on the HSE during mantle melting, despite their relatively low abundance in the upper mantle (e.g., Mitchell and Keays, 1981; Luguet et al., 2003). Mantle sulphides include refractory monosulphide solid solution (MSS) and interstitial Cu-rich sulphides; these phases usually control the abundance of the HSE in the upper mantle (e.g., Alard et al., 2000; Bockrath et al., 2004). Fractionation of the HSE during mantle melting is driven by partitioning between the MSS and sulphide melts, which are represented by the interstitial Cu-rich sulphides. The IPGEs are thought to partition into the MSS under moderate oxygen activities and in the presence of volatiles such as H_2O (Mungall, 2002, Mungall et al., 2006; Dale et al. 2012; Botcharnikov et al, 2013), while the PPGEs are more likely to partition into the sulphide melt. However, partitioning between MSS and sulphide melts does not account for some characteristics of Pd, Pt and Au concentrations in depleted mantle peridotites (Fischer-Godde et al, 2011).

Metal alloys of Os, Ir and Ru form in the mantle when relatively high degrees of melting have exhausted sulphides in residual peridotites. Sufficiently high degrees of melting are thought to occur during production of MORB (e.g., Klein and Langmuir, 1987; Fonseca et al., 2011, 2012, Mungall and Brenan, 2014). Therefore, alloys might host a significant proportion of the IPGEs in the depleted mantle beneath mid ocean ridges. However, if the protoliths to the Serra di Pigno samples were from slow-spreading or OCT settings, then melt extraction might not have been extensive, and the sulphides would have hosted the HSE.

It is difficult to determine the dominant control on the distribution of the HSE in the protoliths to the samples in this study because the effects of serpentinisation, subduction-zone metamorphism, and exhumation might have overprinted the earlier record. However, given that the

protoliths are similar to peridotites from the KFZ and the IL, it is likely that sulphides were present in the protoliths and sulphide phases would have controlled the distribution of the HSE prior to serpentinisation.

Mineral-scale HSE distribution in the Serra di Pigno serpentinites

Prograde sulphides and sulphides associated with exhumation hosted within subducted serpentinites from Serra di Pigno have lower HSE concentrations than sulphides from the KFZ, a slow spreading margin (Luguet et al., 2003; Alard et al., 2005, Fig. 5b and c) and the IL, an OCT setting (Luguet et al., 2004, Fig. 5b and c). Ruthenium concentrations are consistently higher relative to the other IPGEs (Os and Ir), and Pd concentrations are lower in the texturally late pentlandite (pn3) in CO13-33 (proximal: Fig. 5b) than in earlier sulphides.

Notably, three hydrothermal sulphide grains from the IL also contain lower PGE contents than those in primary IL and KFZ sulphides (Fig. 5b and c, Luguet et al., 2004). These hydrothermal sulphides from IL have similar Os and Ir concentrations to the Ni-rich sulphides from Serra di Pigno but lower Ru concentrations. It is therefore possible that the lower HSE contents in the Serra di Pigno samples are associated with a hydrothermal overprint. However, the overall HSE pattern shown by the Serra di Pigno serpentinites differs to that of the hydrothermal IL sulphides, with higher concentrations of the IPGE (Fig. 5b and c). Therefore, the attribution of lower PGE contents to a hydrothermal overprint is likely to be an oversimplification, and other processes must be considered.

To summarise, the complex HSE patterns shown by the sulphides suggest that the HSE might have been mobilised during metamorphism on small length scales (< dm), with no evidence for HSE mobility on the rock sample scale or greater (as discussed above). The most likely cause of this mobilisation is changes to the HSE-hosting assemblage driven by changes in pressure, temperature,

fluid infiltration, and redox conditions. Mechanisms for the redistribution of the HSE on a mineral scale are discussed below, in the context of processes that occur during subduction and exhumation.

Evolution of sulphur and oxygen activities during metamorphism

The stability of mineral phases that host the HSE are sensitive to aO_2 and aS_2 (e.g., Foustoukos et al., 2015), and the variance of the oxide–sulphide assemblage indicates whether aO_2 and aS_2 were internally or externally buffered, so it is useful to constrain these parameters. Evans et al. (2017) present activity-activity diagrams of oxide and sulphide stability as a function of at high pressure (2 GPa, 555 ºC) in the system Ni–Fe–O–S. Assemblages that can buffer aO_2 and aS_2 include awaruite–heazlewoodite–magnetite–pentlandite, pyrite–pyrrhotite–magnetite, and hematite–pyrite–magnetite. The sulphide ± magnetite assemblages in the Serra di Pigno and Capu Covoli samples (see petrography section) were plotted on the activity–activity diagram (Fig. 6). Peak temperatures and pressures at Serra di Pigno (blueschist–eclogite facies; 414°C–471°C and 1.3–2.6 GPa; Vitale Brovarone, 2013) were lower than at Capu Corvoli (eclogite facies; estimated 435°C–507 ºC and 1.9–2.6 GPa; Ravna et al., 2010; Vitale Brovarone et al., 2011; 2013). However, the relative positions of the buffering assemblages, with the exception of the millerite-vaesite reaction, are unaffected by a pressure increase from 0.5 to 2 GPa (Evans et al., 2017). Consequently, trends of aO_2 and aS_2 for specific sulphide assemblages are not sensitive to differences in P-T conditions recorded at the two localities. Kamacite, which was observed in CO13-33 (proximal MGMQ), was not included in the phase diagram calculations; however it can be assumed that kamacite + magnetite records similar aS_2, but slightly lower aO_2 than awaruite + magnetite (Frost, 1985; Schwazenbach et al., 2012; Foustoukos et al., 2015).

The oxide and sulphide mineral assemblages of the Serra di Pigno serpentinites are generally low variance, consisting of pentlandite + magnetite ± pyrite or pentlandite + magnetite + heazlewoodite (Fig. 6a and b). The low variance suggests that assemblages and fluid composition

were rock-buffered during metamorphism. Therefore, the composition of the fluids infiltrating the rocks and the mineralogical evolution of the Serra di Pigno serpentinites were controlled by equilibrium between the fluid and the mineral phases (e.g., Goodge and Holdaway, 1995). The Serra di Pigno serpentinites record both increases and decreases in aO_2 and aS_2 during progressive metamorphism and do not show systematic trends in aO_2–aS_2 space as a function of metamorphic stage, mineral assemblages, or proximity to other lithologies (Fig. 6a and b).

The hybrid ultramafic/mafic samples from Capu Corvoli plot at higher aS_2 than the Serra di Pigno serpentinites (Fig. 6c). Mafic rocks generally contain more sulphur than serpentinites prior to subduction (e.g., Delacour et al., 2008), so the proximity of the hybrid rocks to metagabbro could explain the increased aS_2. However, the sulphur content of the metagabbro that lies between hybrid rock samples CO14-03 and CO14-04 (670 ppm) is similar to that of the mean of the two hybrid samples (685 ppm S: Table 1). It is therefore likely that the metagabbro lost sulphur during metamorphism, and that the sulphur was mobilised into the hybrid rocks, increasing aS_2. The oxide–sulphide components of the mineral assemblage in CO14-03 show a high variance, with one oxide or sulphide phase predicted to be stable at any given time (i.e., magnetite or pyrite, Fig. 6c). This suggests that these rocks were fluid-buffered during metamorphism. There is some evidence that CO14-04 was initially rock-buffered, with two or three phases, but transformed to a fluid-buffered assemblage with one phase (py2) during the transition from prograde to early retrograde metamorphism. This scenario is consistent with fluid infiltration during exhumation.

The elevated aO_2 in the hybrid rocks could be attributed to an increase in redox budget driven by loss of hydrogen-bearing fluids during prograde metamorphism. However, the assemblages suggest that aS_2 and aO_2 increased, not only during prograde metamorphism, but also during exhumation, which is more consistent with the infiltration of oxidised fluids during exhumation than with prograde loss of H_2-bearing fluids. The oxidised fluids could have been provided by dehydration of mafic and metasedimentary rocks at the blueschist-eclogite transition deeper in the

subduction zone, consistent with the results of Evans et al. (2014), and with the proposal that this transition is a major source of metasomatic fluid that drive hybridisation (Spandler et al., 2008).

Could sulphur addition explain low concentrations of the HSE in sulphides?

The lower concentrations of the HSE in high-pressure sulphides compared with their seafloor precursors could be explained by an increase in bulk-rock sulphur with a consequent increase in the mode of sulphides, which would dilute the HSE concentrations in the sulphides. This is a plausible explanation for samples with a high bulk sulphur concentration, such as the sample proximal to other lithologies (CO13-33, 1100 ppm S) and the hybrid Capu Corvoli rocks, where the chlorite schist (CO14-03) and talc schist (CO14-04) have S concentrations of 430 ppm and 940 ppm, respectively. Further evidence for sulphur addition exists in the form of primary and/or seafloor chromite surrounded by hz1 in CO13-31 (distal), and chromite included within pn2 in CO13-55 (proximal MGCS). However, the bulk sulphur contents of serpentinite samples CO13-31 and CO13-55 are only 300 ppm and 200 ppm, respectively.

A review of the sulphur content of serpentinites from slow spreading and OCT settings from the Ligurian Alps and Voltri Massif in the Northern Apennines, Italy suggest that pre-subduction sulphur contents are variable (~200–1400 ppm for the Northern Apennines), and that the variability is retained during subduction (~130–2400 ppm for the Voltri Massif: Alt et al., 2012). It is therefore difficult to constrain the pre-subduction sulphur content or assess the likelihood of sulphur addition. Nevertheless, a lack of systematic trends between sulphur and PGE contents observed in these samples, and from the Ligurian Alps (Luguet et al., 2004) suggest that PGE concentrations are not controlled by solely by addition and removal of sulphur, and that alternative explanations are required.

Could non-sulphide mineral hosts explain low HSEs in sulphides?

An alternative explanation for the low HSE concentrations in sulphides is the presence of other minerals that host the 'missing' HSE. Under some conditions, the IPGE (Os, Ir and Ru) are highly compatible, and Pd and Pt are moderately compatible, in primary Cr-rich spinel phases (Hart and Ravizza 1996; Puchtel and Humayun 2001). Sequestration of the HSE within these phases could account for the lower HSE concentrations in the sulphides. However, the concentrations of the HSE in spinels are low, except for one grain in the serpentinite sample CO13-31 (distal, Electronic Appendix 9), and the porous texture of some spinel grains and the magnetite rims on Cr-rich spinel suggests that primary spinel has been altered to more Fe^{3+}-rich compositions. Furthermore, Ru, Ir and Rh concentrations are low in the spinels from Serra di Pigno and Capu du Corvoli, which is inconsistent with the partitioning of Ru, Ir, and Rh into Fe^{3+}-rich spinels (Brenan et al., 2012). Thus, it is unlikely that the low HSE concentrations in sulphides can be attributed to sequestration of HSEs into spinel.

Metal alloys are another candidate that might host the 'missing' HSEs. Platinum-bearing alloys were observed on the rim of two heazlewoodite grains in serpentinite CO13-31 (distal), and near the rim of a py1 grain within the CO14-04 (talc schist). Kamacite was observed in balangeroite veins in a serpentinite sample proximal to other lithologies (CO13-33). Alloy stability is consistent with the inferred aO_2 conditions (Fig. 6). Platinum-bearing alloys are considered to be stable under low aO_2 (Mungall and Brenan, 2014), and Pt exsolves from sulphide under low aS_2 (Peregoedova et al., 2004), so the observed Pt-bearing alloys on the edge of sulphides reflect low aO_2 and aS_2 and a decrease in oxidation state post-sulphide growth. Therefore, the presence of HSE-bearing alloys might account for variable Pt concentrations in the Ni sulphides and the low Pt concentrations in pyrite in the Capu Corvoli rocks, relative to those in the inferred protoliths. The low concentration of Au in Ni-rich sulphides from the Internal Ligurides, Italy, was attributed to the presence of native Au

grains (Luguet et al., 2004; Lorand et al., 2010), although native Au was not observed in the samples of the present study.

An explanation for decoupling between Os–Ir and Ru during metamorphism

Whole-rock Ru concentrations in all Serra di Pigno serpentinite samples are similar to PUM, whereas the Ni-rich sulphides in the serpentinites (hz1, pn2 and pn3) are enriched in Ru relative to the other IPGEs, Os and Ir, compared to sulphides in the KFZ and IL protoliths (Fig. 5b and c). These observations are consistent with decoupling between Ru and Os–Ir on length scales smaller than that of a fist-sized sample. Possible explanations for the decoupling include destabilisation of IPGE-bearing spinel, differential mobilisation in an oxidising fluid, and sequestration of Os and Ir into metal alloys.

The IPGEs are compatible in primary spinel, hence alteration of these spinels during seafloor alteration and/or subduction would release Os, Ir, and Ru. Indeed, the low concentrations of IPGE in the altered spinels in the studied samples (Electronic Appendix 9) suggest that spinel does not host the IPGE in the Alpine Corsican samples. Ruthenium is more sensitive to the chromite content of spinel than the other IPGE, and Ru concentrations in chromite are up to ten times that of the other PGE (Pagé and Barnes, 2016), therefore the preferential release of Ru from spinel could produce Ru-rich sulphides. However, the Fe^{3+}-rich spinels are uniformly depleted in the IPGE, hence alteration of primary spinels is unlikely to have had a substantial influence on the Ru concentrations of sulphides.

Alternatively, Ru can be decoupled from Ir by transport in a relatively oxidised, sulphur-bearing fluid; Ru occurs as the RuO_3 species in relatively oxidising conditions, while Ir remains immobile (Wood, 1987). However, Os is also mobile under oxidised conditions (Wood, 1987), so oxidising fluids would separate Ru and Os from Ir, rather than Ru from Os and Ir.

A further possibility is provided by the formation of metal alloys. The production of Os, Ir, and Pt-rich metal alloys under reducing conditions (Foustoukos et al., 2015) and/or low aS_2 (Fonesca et al., 2009, 2012; Gonzaléz Jimenéz et al., 2012), would decouple Os and Ir from Ru, and the Ru could be sequestered by sulphides. Pt-bearing alloys were observed (see above) but Os–Ir alloys were not. However, such alloys are minute and rare, therefore they might have been present even if they were not observed. Furthermore, the Ru content of heazlewoodite (3.6–4.1 ppm) is generally higher than that of pentlandite (1.7–2.5 ppm), with the exception of one pentlandite grain (pn3 grain s4-3). Heazlewoodite is stable at a lower aS_2 than pentlandite (Fig. 6), and low aS_2 is required for alloy formation, hence this observation is consistent with IPGE decoupling and alloy formation at low aS_2.

Pd enrichment in the Serra di Pigno sulphides

Pentlandite related to the onset of exhumation (pn2, CO13-33, proximal to metagabbro and metaquartzite), inferred to be associated with exhumation in the Serra di Pigno serpentintes, have higher concentrations of Pd compared to earlier sulphides (hz1, CO13-31, distal) and later pentlandite grains (pn3, CO13-55, proximal to metagabbro and calc schist), although compared to the seafloor KFZ and IL sulphides, Pd concentrations are higher in hz1 (CO13-31, distal). One possible explanation for these observations is that the Pd concentration is controlled by the sulphide composition (i.e. Ni, S or Fe content). However, the notable difference in Pd concentration between pn2 and pn3 suggests other mechanisms, such as Pd mobilisation, could be more significant.

There is limited evidence for Pd mobilisation on the whole-rock scale (see above), therefore any mobilisation must have been on short length scales. It is possible that Pd was already sequestered in sulphide phases when pn3 grew in CO13-55 (proximal MGCS), which would explain the low Pd concentrations, if equilibration occurred only on limited length scales. This suggestion is consistent

with the low fluid-rock ratios inferred from the aO_2–aS_2 diagrams (Fig. 6a and b), and the heterogeneous but relatively high Pd concentrations in pn2 in CO13-33.

Notably, Pd/Ru = ~1 in the whole rock, whereas Pd/Ru =~0.001–0.002 in pn2, which is the most Pd-rich sulphide. This suggests that a phase with high Pd/Ru is present, but was not analysed. Potential candidates include earlier sulphides, that are too small to analyse, and other Pd-bearing minerals; for example, Pd-bearing alloy grains as observed within samples from Monte Maggiore, in the north of Cap Corse (Ohnenstetter et al., 1992). Pd-rich alloys are rare under mantle conditions, even under very low aS_2, therefore Pd is most likely to partition into sulphide phases (Mungall and Brenan, 2014). On the other hand, the effects of fluid infiltration at the onset of exhumation under high pressure conditions on the distribution of Pd is not known. Indeed, it has been suggested such Pd-rich alloys form as a result of Cl-bearing fluids enriched in Pd and other metals, migrating to cooler or more oxidised zones (Ohnenstetter et al., 1992). A similar mechanism could be responsible for Pd-alloy formation in a scenario, where fluids derived from the devolatilisation of the downgoing slab migrated from greater to shallower depths. However, given that Pd is not mobilised on a whole rock scale, it is more likely that Pd has been retained in earlier sulphides, consistent with the high concentration of Pd in hz1, a prograde to peak sulphide phase (CO13-31, distal, Table 2, Fig. 5a). These observations are consistent with the hypothesis that Pd was retained in the Serra di Pigno serpentinites during subduction.

The role of alloys as hosts of HSE: mass balance calculations

The formation and stability of alloy grains is a favoured hypothesis to explain the observed distribution of HSEs in the Serra di Pigno samples and a small number of alloy grains were observed in the samples. Two Pt-bearing alloy grains were observed in CO13-31 (distal) and kamacite is present in balangeroite veins in CO13-33 (proximal to metagabbro and metaquartzite) but none were observed in CO13-55 (proximal to metagabbro and calc schist), despite utilising high resolution

feature mapping techniques and assessing laser ablation time resolved profiles for peaks of these elements within the sulphide grains. It is therefore possible that alloys are present but in such low modes that they are not always observed. To test this hypothesis, mass balance calculations were carried out to determine the volume % of the alloy in the rock, and the probability of observing them in a single thin section. Note that these calculations may overestimate the probability of alloy observation, because small sulphide phases which were not analysed by LA-ICP-MS may contain some of the HSE budget.

Based on the few observed alloys in thin section, the area of individual Pt-bearing alloys is 25 μm^2 or less, with the smallest observed Pt-bearing alloy on the rim of heazlewoodite ~2 μm^2 in size. The size of the thin section is ~1.24 x 10^9 μm^2. If the area of the alloy grains is taken as 25 μm^2, the mode of one alloy grain is 2 x 10^{-6} vol%. The average density of alloys is taken as 12 g/cm^3, though this value could be between 8 and 20 g/cm^3, depending on the composition of the alloy. Most of the thin section is comprised of serpentine in the case of the Serra di Pigno samples, or talc and chlorite in the case of the Capu Corvoli samples, where all three phases have an average specific gravity of ~2.75 g/cm^3, so the average density of alloys would be ~4 times that of serpentine. By weight, the mass of the alloy in a thin section containing a 25 μm^2 alloy grain would therefore be 8.73 x 10^{-6} wt%. Using the example of CO13-31 (distal), which has a total concentration of 38 ppb or 3.8 x 10^{-6} wt% HSE, the bulk HSE content provides only ~40% of the mass required to give a 25 μm^2 in each section, and, on average, one grain would be observed if two or more thin sections were examined. If the alloy grains were smaller, at least one grain would be expected to be present in each thin section, although such small grains might be difficult to detect. For example, the smallest alloy grain detected is 2 μm^2 giving a mode of 1.61 x 10^{-7}vol%, and mass of 7.03 x 10^{-7} wt%, where the total HSE budget is ~540% of the mass of the alloy; therefore, approximately five grains would be expected to be observed in each thin section. Alloys with a higher density, for example, pure Os-Ir alloys, would have a higher density of ~20 g/cm^3 (e.g., Walker et al., 2005) so the likelihood of observing such an

alloy would be lower. For example, taking the alloy area of ~25 μm^2, with a mass of 1.45 x 10^{-5} wt%, the total HSE concentration would account for ~26% of the mass of the alloy, thus one grain would be seen approximately every four thin sections.

To summarise, the mass fraction of alloys depends on the composition, size, and density of the alloy, where alloys of lower density would be of higher mode compared to those with a higher density. On the other hand, high density alloys would require analysis of multiple mounts of the same sample via automated mapping techniques, which is beyond the scope of this study.

An explanation for high rhenium in the hybrid rocks

Rhenium is elevated in CO14-04 relative to PUM and slow-spreading centre serpentinites. Rhenium is one of the least compatible HSEs in the mantle (Brenan 2008; Fonseca et al., 2007; Mallmann and O'Neill, 2007), and is transferred into crustal rocks such as gabbros and metabasalts by melting. Therefore, Re from mafic rocks might have been added to the ultramafic rocks by fluids produced by dehydration of nearby mafic rocks, consistent with the loss of Re during prograde metamorphism of mafic rocks that has been documented in other locations (Becker, 2000; Dale et al., 2007, 2009; Penniston-Dorland et al., 2012). In this case, the high Re concentrations record fluid-mediated mixing between components derived from gabbroic and ultramafic rocks in the subduction channel. This proposal is consistent with the hybrid nature of CO14-04. The shearing of the metagabbro and serpentinite observed in the field is consistent with deformation during prograde metamorphism (see Geological Setting), and might have facilitated pervasive fluid flow between the lithologies.

Alternatively, or additionally, experimental work has demonstrated that Re partitioning is redox-sensitive at the high temperatures found in the mantle. Under these conditions, and at high oxygen activities, Re can act as a lithophile element rather than as a chalcophile element (Fonseca et al., 2007; Mallmann and O'Neill, 2007), therefore low oxygen activities might be related to high Re

concentrations. However, it is unlikely that low oxygen activity can explain the high Re concentrations in py2 from the Capu Corvoli hybrid rocks because: (i) the experimental conclusions do not necessarily imply elevated Re at low oxygen activity; (ii) the temperatures at which pyrite grew are much lower than those of the experiments; (iii) the presence of pyrite suggests that oxygen activity is higher, rather than lower, than in the other rocks analysed for this study; and (iv) the concentration of Re in magnetite was below the limit of detection (Electronic Appendix 9), even though it has been demonstrated that Re is compatible in magnetite under oxidising conditions (Righter & Hauri, 1998; Righter and Downs, 2001). Therefore, conditions were clearly insufficiently oxidising and/or Re was not available at the time of magnetite growth. The higher concentrations of Re in the rim compared to the core of py2 grains in the talc schist sample (CO14-04; Table 3) implies that Re-bearing fluids infiltrated the rock during exhumation.

Implications for cycling of the HSE in subduction zones

The findings of this study suggest that the HSE were not mobilised on length scales of more than a few centimetres in the serpentinites at blueschist–eclogite facies grade. The sub-arc mantle is considered to be contain elevated concentrations of Pt and Pd, compared to mantle elsewhere (McInnes et al., 1999; Kepezhinskas et al., 2002; Lee, 2002). However, based on the results of this study, and those of a previous study by Blanco-Quintero et al. (2011), the HSE are not mobilised during metamorphism to blueschist–eclogite facies. Instead, basaltic crust might contribute to the Pd and Pt budget of the sub-arc mantle; Dale et al. (2009) suggest that Pt is released from the basaltic component of the slab, and Pd is released from both the gabbroic and basaltic crust.

Hybridisation of lithologies is a potential mechanism to transfer the HSE to the sub-arc mantle. High concentrations of Re in the talc schist sample, and Ru and Ir depletion in the chlorite schist sample, suggest that mobilisation of these elements are possible in hybridised rocks. Mobilisation would be favoured by the chemical potential gradients that exist between rocks of

different types, and by focusing of fluids along lithological contact. Shearing within the metagabbro would also have facilitated pervasive fluid flow, hence Re mobilisation from the metagabbro could have occurred on longer length scales than those accessible in this study and the transfer of Re via fluids derived from the slab could provide a mechanism for Re enrichment in arc magmas (e.g., Sun et al., 2004). Rhenium transfer to the sub-arc mantle and/or deep mantle and fractionation of Os from other IPGE could have consequences for the feasibility of the Re-Os isotope system as tracers of recycled crustal material in these reservoirs (e.g., Dale et al., 2009), and requires further investigation.

Hybrid rocks between the sub-arc mantle and the slab provide a potential source of elements for the sub-arc mantle (Marschall and Schumacher, 2012). Regardless of the precise mechanism, anomalous Re and the fractionation of IPGE in the hybrid rocks could be inherited by the sub-arc mantle, and subsequently arc magmas (e.g., Dale et al., 2009; Marschall & Schumacher, 2012; Penniston-Dorland et al., 2014). Additional research is necessary to assess these effects.

A number of features within the data are best explained by the presence of HSE-bearing alloys. These include the low HSE concentrations in the Serra di Pigno serpentinite sulphides relative to those in plausible protoliths, the decoupling between Os–Ir and Ru, and the variable Pt concentrations in the sulphides. If alloys are present, then the HSE might be mobilised from sulphide to alloy hosts in response to desulphurisation, and/or change in redox conditions or metamorphic conditions; the consequences of these shifts for the metamorphic cycling of HSEs are unknown. Some alloys were recognised in this work, but their small size and low modal abundance has meant that they are rare and difficult to detect. However, their potential significance as a repository for these rare phases means that further work is necessary to detect and characterise these phases.

CONCLUSIONS

Sulphide and oxide parageneses of high-pressure serpentinites provide a wealth of information regarding changes in aO_2, aS_2, and the HSE distribution during metamorphism. Detailed observations of samples from Alpine Corsica reveals a range of trajectories in $aO_2 - aS_2$ space, with $aO_2 - aS_2$ both increasing and decreasing as metamorphism progresses, although changes are not systematically linked to the proximity of specific lithologies in the blueschist-eclogite facies terrain. Low variance assemblages suggest that sulphide assemblages were controlled by internal rock buffering processes. In contrast, hybrid rock samples, associated with blueschist-eclogite to eclogite terrains, record higher $aO_2 - aS_2$ than the Serra di Pigno serpentinites, which is interpreted as a record of fluid infiltration from the adjacent metagabbros.

The HSE were not mobilised on length scales greater than a few centimetres. In contrast, the Capu Corvoli hybrid mafic/ultramafic samples show evidence for Re, Ru and/or Ir mobilisation, which is attributed to fluid mediated transfer from the proximal metagabbro. With the exception of Re concentrations, the lower HSE concentrations in the Capu Corvoli sulphides related to advanced stages of exhumation could be attributed to HSE dilution by sulphur introduction during the onset of exhumation. However, sulphur addition does not explain the low HSE contents in sulphides within Serra di Pigno.

Alloys, which were observed in multiple samples, may provide an important host for the HSE throughout the subduction cycle. For example, the Ru-rich nature of the Ni-rich sulphides is proposed to be a result of exsolution of Os and Ir alloys, although the conditions of HSE alloy formation (e.g., Os-Ir and Pt alloys) are not fully understood and alloys are difficult to detect. Further investigations on alloy formation is necessary to improve our knowledge of the hosts of the HSE in subduction ultramafic rocks, and to constrain the evolution of redox conditions during subduction and exhumation.

FUNDING

This work was supported by an Australian Research Council (ARC) Future Fellowship (FF12000579) to K.E., and a Curtin International Postgraduate Research Scholarship (CIPRS) to R.J.C.

ACKNOWLEDGEMENTS

Luke Daly and Sarah Hayes are thanked for the Capu Corvoli rock samples and for discussions on field observations. Malcolm Roberts is thanked for his assistance with the JEOL 8530 WDS microprobe at the Centre for Microscopy, Characterisation and Analysis, the University of Western Australia. Elaine Miller is thanked for her help with feature mapping on the Tescan Mira 3 and Kelly Merigot is thanked for assistance with the TIMA at the JdLC Microscopy and Microanalysis Facility (MMF), Curtin University. Richard Holdsworth at Intertek Genalysis is thanked for information on certified reference materials and further details on NiS-FA for whole rock PGE analysis. Chris Ballhaus is thanked for proposing the collaboration between the Geohistory Facility (JdLC, Curtin University) and Bonn University. We thank editors J. Mungall and A. Audetat, and reviewers S. Aulbach, T Pettke and an anonymous reviewer for their thorough and constructive reviews of this paper. SMR acknowledges the ARC Core to Crust Centre of Excellence (COE) grant (CE1101017). The TIMA instrument was funded by a grant from the Australian Research Council (LE140100150) and is operated by the John de Laeter Centre at Curtin University with the support of the Geological Survey of Western Australia, University of Western Australia and Murdoch University.

REFERENCES

Alard, O., Griffin, W. L., Lorand, J. P., Jackson, S. E., & O'Reilly, S. Y. (2000). 'Non-chondritic distribution of the highly siderophile elements in mantle sulphides'. *Nature*, **407**(6806), 891.

Alard, O., Luguet, A., Pearson, N. J., Griffin, W. L., Lorand, J. P., Gannoun, A., ... & O'Reilly, S. Y.

(2005). ‘In situ Os isotopes in abyssal peridotites bridge the isotopic gap between MORBs and their source mantle’. *Nature*, **436**(7053), 1005.

Alt, J. C., Shanks III, W. C., Crispini, L., Gaggero, L., Schwarzenbach, E. M., Früh-Green, G. L., & Bernasconi, S. M. (2012). ‘Uptake of carbon and sulfur during seafloor serpentinization and the effects of subduction metamorphism in Ligurian peridotites’. *Chemical Geology*, **322**, 268-277.

Andrews, D. R., & Brenan, J. M. (2002). ‘The solubility of ruthenium in sulfide liquid: implications for platinum group mineral stability and sulfide melt–silicate melt partitioning’. *Chemical Geology*, **192**(3-4), 163-181.

Aulbach, S., Stachel, T., Seitz, H. M., & Brey, G. P. (2012). ‘Chalcophile and siderophile elements in sulphide inclusions in eclogitic diamonds and metal cycling in a Paleoproterozoic subduction zone’. *Geochimica et Cosmochimica Acta*, **93**, 278-299.

Baker, J. A., & Jensen, K. K. (2004). ‘Coupled 186Os–187Os enrichments in the Earth’s mantle–core–mantle interaction or recycling of ferromanganese crusts and nodules?’. *Earth and Planetary Science Letters*, **220**(3-4), 277-286.

Barra, F., Gervilla, F., Hernández, E., Reich, M., Padrón-Navarta, J. A., & González-Jiménez, J. M. (2014). ‘Alteration patterns of chromian spinels from La Cabaña peridotite, south-central Chile’. *Mineralogy and Petrology*, **108**(6), 819-836.

Barnes, J. D., Beltrando, M., Lee, C.-T. A., Cisneros, M., Loewy, S. & Chin, E. (2014), ‘Geochemistry of Alpine serpentinites from rifting to subduction: A view across paleogeographic domains and metamorphic grade’. *Chemical Geology* **389**, 29–47.

Barnes, S. J. (2000), ‘Chromite in komatiites, II. Modification during greenschist to mid-amphibolite facies metamorphism’, *Journal of Petrology* **41**(3), 387–409.

Barnes, S. J. & Liu, W. (2012), 'Pt and Pd mobility in hydrothermal fluids: evidence from komatiites and from thermodynamic modelling', *Ore Geology Reviews* **44**, 49–58.

Barnes, S. J., Mungall, J. E., & Maier, W. D. (2015). ‘Platinum group elements in mantle melts and mantle samples’. *Lithos*, **232,** 395-417.

Barnes S-J, Naldrett AJ, Gorton MP (1985) ‘The origin of the fractionation of platinum-group elements in terrestrial magmas’. *Chemical Geology* **53**, 302–323

Becker, H. (2000), 'Re–Os fractionation in eclogites and blueschists and the implications for recycling of oceanic crust into the mantle', *Earth and Planetary Science Letters* **1773**, 287–300.

Becker H., Horan M.F., Walker R.J., Gao S., Lorand J.-P. and Rudnick R.L. (2006) ‘Highly siderophile element composition of the Earth’s primitive upper mantle: constraints from new data on peridotite massifs and xenoliths’. *Geochimica et Cosmochimica Acta*, **70**, 4528–4550.

Beltrando, M., Compagnoni, R. & Lombardo, B. (2010), '(Ultra-) High-pressure metamorphism and orogenesis: An Alpine perspective', *Gondwana Research* **18**(1), 147–166.

Blanco- Quintero, I. F., Proenza-Fernández, A., García-Casco, A., Tauler, E. & Galé Medina, S.

(2011), 'Serpentinites and serpentinites within a fossil subduction channel: La Corea mélange, eastern Cuba', *Geologica Acta* **9**(3).

Bliss, N. & MacLean, W. (1975), 'The paragenesis of zoned chromite from central Manitoba', *Geochimica et Cosmochimica Acta* **39**(6), 973–990.

Bockrath, C., Ballhaus, C., Holzheid, A. (2004) 'Fractionation of the platinum-group elements during mantle melting'. *Science* **305**:1951-1953

Botcharnikov, R. E., Holtz, F., Mungall, J. E., Beermann, O., Linnen, R. L., & Garbe-Schönberg, D. (2013). 'Behavior of gold in a magma at sulfide-sulfate transition: Revisited'. *American Mineralogist*, *98*(8-9), 1459-1464.

Bragagni, A., Van Acken, D., Fonseca, R. O., Speelmanns, I. M., Wainwright, A. N., Heuser, A., Nowell, G.M. & Luguet, A. (2018). 'Re-Os and HSE in individual base metal sulphide grains: Evaluating micro-analytical procedures using a sulphide reference material'. *Chemical Geology* **493**, 426–440.

Brenan, J. M. (2008). 'Re–Os fractionation by sulphide melt–silicate melt partitioning: a new spin'. *Chemical Geology*, *248*(3), 140-165.

Brenan, J. M., & Andrews, D. (2001). 'High-temperature stability of laurite and Ru–Os–Ir alloy and their role in PGE fractionation in mafic magmas'. *The Canadian Mineralogist*, **39**(2), 341-360.

Brenan, J.M., Finnegan, C.F., McDonough, W.F. (2012), 'Experimental constraints on the partitioning of Ru, Rh, Ir, Pt and Pd between chromite and silicate melt: the importance of ferric iron', *Chemical Geology*, **302–303**, 16–32.

Burton, K.W., Schiano, P., Birck, J.L., Allègre, C.J. (1999) 'Osmium isotope disequilibrium between mantle minerals in a spinel-lherzolite'. *Earth Planet Sci Lett* **172**:311-322

Burton, K. W., Schiano, P., Birck, J. L., Allegre, C. J., Rehkämper, M., Halliday, A. N., & Dawson, J. B. (2000). 'The distribution and behaviour of rhenium and osmium amongst mantle minerals and the age of the lithospheric mantle beneath Tanzania'. *Earth and Planetary Science Letters*, **183**(1-2), 93-106.

Burton, K. W., Gannoun, A., Birck, J. L., Allègre, C. J., Schiano, P., Clocchiatti, R., & Alard, O. (2002). 'The compatibility of rhenium and osmium in natural olivine and their behaviour during mantle melting and basalt genesis'. *Earth and Planetary Science Letters*, **198**(1-2), 63-76.

Capobianco, C. J. & Drake, M. J. (1990) 'Partitioning of ruthenium, rhodium, and palladium between spinel and silicate melt and implications for platinum-group element fractionation trends'. *Geochim Cosmochim Acta* **54**:869-874

Capobianco, C.J., Hervig, R.L, Drake, M.J. (1994) 'Experiments on crystal/liquid partitioning of Ru, Rh and Pd for magnetite and hematite solid solutions crystallized from silicate melt'. *Chemical Geology* **113**:23-43

Chan, T.K., & Finch, I.J., (2001). 'Determination of platinum-group elements and gold by inductively coupled plasma mass spectrometry'. In: Australian Platinum Conference, Perth, Western

Australia.

Colás, V.; González-Jiménez, J. M.; Griffin, W. L.; Fanlo, I.; Gervilla, F.; O'Reilly, S. Y.; Pearson, N. J.; Kerestedjian, T. & Proenza, J. A. (2014), 'Fingerprints of metamorphism in chromite: New insights from minor and trace elements', *Chemical Geology* **389**, 137–152.

Crossley, R. J., Evans, K. A., Jeon, H., & Kilburn, M. R. (2018). 'Insights into sulphur cycling at subduction zones from in-situ isotopic analysis of sulphides in high-pressure serpentinites and 'hybrid' samples from Alpine Corsica'. *Chemical Geology*, **493**, 359–378.

Dale C.W., Macpherson C.G., Pearson D.G., Hammond S.J., Arculus R.J. (2012) 'Inter-element fractionation of highly siderophile elements in the Tonga Arc due to flux melting of a depleted source'. *Geochimica et Cosmochimica Acta* **89**, 202–225

Dale, C., Burton, K., Pearson, D., Gannoun, A., Alard, O., Argles, T. & Parkinson, I. (2009), 'Highly siderophile element behaviour accompanying subduction of oceanic crust: whole rock and mineral-scale insights from a high-pressure terrain', *Geochimica et Cosmochimica Acta* **73**(5), 1394–1416.

Dale, C., Gannoun, A., Burton, K., Argles, T. & Parkinson, I. (2007), 'Rhenium–osmium isotope and elemental behaviour during subduction of oceanic crust and the implications for mantle recycling', *Earth and Planetary Science Letters* **253**(1), 211–225.

Danyushevsky, L., Robinson, P., Gilbert, S., Norman, M., Large, R., McGoldrick, P. & Shelley, M. (2011), 'Routine quantitative multi-element analysis of sulphide minerals by laser ablation ICP-MS: Standard development and consideration of matrix effects', *Geochemistry: Exploration, Environment, Analysis* **11**(1), 51–60.

Debret, B., Koga, K. T., Nicollet, C., Andreani, M., & Schwartz, S. (2014). 'F, Cl and S input via serpentinite in subduction zones: implications for the nature of the fluid released at depth'. *Terra Nova*, *26*(2), 96-101.

Debret, B., & Sverjensky, D. A. (2017). 'Highly oxidising fluids generated during serpentinite breakdown in subduction zones'. *Scientific reports*, **7**(1), 10351.

Deschamps, F., Godard, M., Guillot, S., & Hattori, K. (2013). 'Geochemistry of subduction zone serpentinites: A review'. *Lithos*, *178*, 96-127.

Deer, W., Howie, R. & Zussman, J. (1963), 'Rock forming minerals, Sheet Silicates, v. 3', London, Longman Green and Co., 270p.

Delacour, A., Fruh-Green, G. L., Bernasconi, S. M., 2008. 'Sulphur mineralogy and geochemistry of serpentinites and gabbros of the Atlantis Massif (IODP site U1309)' *Geochimica Et Cosmochimica Acta* **72** (20), 5111–5127.

Deschamps, F., Godard, M., Guillot, S. & Hattori, K. (2013), 'Geochemistry of subduction zone serpentinites: A review', *Lithos* **178**, 96–127.

Donovan, J., Kremser, D. & Fournelle, J. (2012), 'Probe for EPMA: acquisition, automation and analysis', *Probe Software, Inc., Eugene, Oregon*.

Ernst, W.G. & Liu, J., 1998. ‘Experimental phase-equilibrium study of Al- and Ti-contents of calcic amphibole in MORB – a semiquantitative thermobarometer’. *American Mineralogist*, **83**, 952–969.

Evans, B. W. & Frost, B. R. (1975), 'Chrome-spinel in progressive metamorphism—a preliminary analysis', *Geochimica et Cosmochimica Acta* **39**(6-7), 959–972.

Evans, K. (2012), 'The redox budget of subduction zones', *Earth-Science Reviews* **113**(1), 11–32.

Evans, K. & Powell, R. (2015), 'The effect of subduction on the sulphur, carbon and redox budget of lithospheric mantle', *Journal of Metamorphic Geology* **33**(6), 649–670.

Evans, K. A., Reddy, S. M., Tomkins, A. G., Crossley, R. J., & Frost, B. R. (2017). ‘Effects of geodynamic setting on the redox state of fluids released by subducted mantle lithosphere’. *Lithos*, **278**, 26-42.

Evans, K., Tomkins, A., Cliff, J. & Fiorentini, M. (2014), 'Insights into subduction zone sulphur recycling from isotopic analysis of eclogite-hosted sulphides', *Chemical Geology* **365**, 1–19.

Faure, M. & Malavielle, J., 1981, ‘Etude structurale d’un cisaillement ductile: le charriage ophiolitique corse dans la région de Bastia’, *Bull. Soc. Géol. Fr.,* **23** (1981), 335–343.

Fischer-Gödde M, Becker H, Wombacher F (2011) ‘Rhodium, gold and other highly siderophile elements in orogenic peridotites and peridotite xenoliths’. *Chemical Geology* **280**, 365-383

Fitzherbert, J. A., Clarke, G. L., Marmo, B., Powell, R., 2004. ‘The origin and P-T evolution of peridotites and serpentinites of NE New Caledonia: prograde interaction between continental margin and the mantle wedge’, *Journal of Metamorphic Geology* **22** (4), 327–344.

Fleet, M., Crocket, J., Liu, M. & Stone, W. (1999), 'Laboratory partitioning of platinum-group elements (PGE) and gold with application to magmatic sulphide–PGE deposits', *Lithos* **47**(1), 127–142.

Frost, B. R., (1985). ‘On the stability of sulphides, oxides, and native metals in serpentinite’. *Journal of Petrology* **26**(1), 31–63.

Frost, B. R. (1991), 'Stability of oxide minerals in metamorphic rocks', *Reviews in Mineralogy and Geochemistry* **25**(1), 469–488.

Fonseca, R.O.C., Mallmann, G., O’Neill, H.S.C., & Campbell, I.H. (2007). ‘How chalcophile is rhenium? An experimental study of the solubility of Re in sulphide mattes’. *Earth and Planetary Science Letters* **260**, 537–548.

Fonseca, R. O. C., Campbell, I.H., O’Neill, H.S.C. & Allen, C.M. (2009). ‘Solubility of Pt in sulphide mattes: Implications for the genesis of PGE-rich horizons in layered intrusions’. *Geochimica et Cosmochimica Acta* **73**, 5764–5777.

Fonseca, R. O. C, Mallmann, G., O'Neill, H. S. C., Campbell, I. H., & Laurenz, V. (2011). ‘Solubility of Os and Ir in sulfide melt: Implications for Re/Os fractionation during mantle melting’. *Earth and Planetary Science Letters*, **311**(3-4), 339–350.

Fonseca, R. O. C., Laurenz, V., Mallmann, G., Luguet, A., Hoehne, N., & Jochum, K.P., (2012). 'New constraints on the genesis and long-term stability of Os-rich alloys in the Earth's mantle'. *Geochimica et Cosmochimica Acta* **87**, 227–242.

Fournier, M., Jolivet, L., Goffé, B., Dubois, R., 1991 'Alpine Corsica metamorphic core complex', *Tectonics,* **10**, 1173–1186.

Foustoukos, D. I., Bizimis, M., Frisby, C. & Shirey, S. B. (2015), 'Redox controls on Ni–Fe–PGE mineralization and Re/Os fractionation during serpentinization of abyssal peridotite', *Geochimica et Cosmochimica Acta* **150**, 11–25.

Gannoun, A., Burton, K. W., Thomas, L. E., Parkinson, I. J., van Calsteren, P., & Schiano, P. (2004). 'Osmium isotope heterogeneity in the constituent phases of mid-ocean ridge basalts'. *Science*, **303**(5654), 70-72.

Gannoun, A., Burton, K. W., Parkinson, I. J., Alard, O., Schiano, P., & Thomas, L. E. (2007). 'The scale and origin of the osmium isotope variations in mid-ocean ridge basalts'. *Earth and Planetary Science Letters*, **259**(3-4), 541-556.

Gervilla, F.; Padrón-Navarta, J.; Kerestedjian, T.; Sergeeva, I.; González-Jiménez, J. & Fanlo, I. (2012), 'Formation of ferrian chromite in podiform chromitites from the Golyamo Kamenyane serpentinite, Eastern Rhodopes, SE Bulgaria: a two-stage process', *Contributions to Mineralogy and Petrology* **164**(4), 643–657.

Gervilla, F., Proenza, J.A., Frei, R., González-Jiménez, J.M., Garrido, C.J., Melgarejo, J.C., Meibom, A., Díaz-Martínez, R. and Lavaut, W., (2005). 'Distribution of platinum-group elements and Os isotopes in chromite ores from Mayarí-Baracoa Ophiolitic Belt (eastern Cuba)'. *Contributions to Mineralogy and Petrology*, **150**(6), 589-607.

González-Jiménez, J. M., Griffin, W. L., Gervilla, F., Kerestedjian, T. N., O'Reilly, S. Y., Proenza, J. A., Pearson, N. J. & Sergeeva, I. (2012), 'Metamorphism disturbs the Re-Os signatures of platinum-group minerals in ophiolite chromitites', *Geology* **40**(7), 659–662.

Goodge, J. W., & Holdaway, M. J. (1995). Rock-buffered fluid evolution of metapelites and quartzites in the Picuris Range, northern New Mexico. *Journal of Petrology*, **36**(5), 1229-1250.

Grieco, G. & Merlini, A. (2012), 'Chromite alteration processes within Vourinos ophiolite', *International Journal of Earth Sciences* **101**(6), 1523–1533.

Groppo, C. & Compagnoni, R. (2007), 'Metamorphic veins from the serpentinites of the Piemonte Zone, western Alps, Italy: a review', *Periodico di Mineralogia* **76**, 127–153.

Harris, L. (1985), Progressive and polyphase deformation of the Schistes Lustrés in Cap Corse, Alpine Corsica, *J. Struct. Geol.,* **7**, 637–650

Hart, S.R. and Ravizza, G.E., (1996). 'Os partitioning between phases in lherzolite and basalt'. *Earth Processes: Reading the Isotopic Code*, pp.123-134.

Jolivet, R.. Dubois, M., Fournier, B., Goffé, A., Michard, C., Jourdan (1990), 'Ductile extension in Alpine Corsica, *Geology*, **18** 1007–1010.

Jolivet, L., Daniel, J.M., Fournier, M., 1991, 'Geometry and kinematics of extension in Alpine Corsica', *Earth Planetary Science Letters*, **104** (1991), 278–291.

Jolivet, L., Faccenna, C., Goffé, B., Mattei, M., Rossetti, F., Brunet, C., Storti, F., Funiciello, C., Cadet, J.P., D'Agostino, N., Parra, T., 1998. 'Mid crustal shear zones in postorogenic extension: examples from the northern Tyrrhenian Sea case', *Journal of Geophysical Research* **103**, 12123–12160.

Kepezhinskas, P., Defant, M. J., & Widom, E. (2002). Abundance and distribution of PGE and Au in the island-arc mantle: implications for sub-arc metasomatism. *Lithos*, *60*(3-4), 113-128.

Kimball, K. L. (1990), 'Effects of hydrothermal alteration on the compositions of chromian spinels', *Contributions to Mineralogy and Petrology* **105**(3), 337–346.

Lahondère, D. & Guerrot, (1997), 'Datation Nd-Sm du métamorphisme éclogitique en Corse alpine: un argument pour l'existence, au Crétacé supérieur, d'une zone de subduction active localisée le long du block corse-sarde. *Géologie de la France* **3**, 3–11.

Lahondère, J.C., Lahondère, D., Lluch, D., Ohnenstetter, M., Dominici, R. & Vautrelle, C., (1992). Carte géol. France (1/50000), feuille Luri (1102). BRGM, Orléans. (50 pp.)

Laird, J., & Albee, A. L. (1981). Pressure, temperature, and time indicators in mafic schist; their application to reconstructing the polymetamorphic history of Vermont. *American Journal of Science*, *281*(2), 127-175.

Lee, C. T. A. (2002). 'Platinum-group element geochemistry of peridotite xenoliths from the Sierra Nevada and the Basin and Range, California'. *Geochimica et Cosmochimica Acta*, **66**(22), 3987-4005.

Li, X. P., Rahn, M., & Bucher, K. (2008). 'Eclogite facies metarodingites–phase relations in the system SiO2-Al2O3-Fe2O3-FeO-MgO-CaO-CO2-H2O: An example from the Zermatt-Saas ophiolite'. *Journal of Metamorphic Geology*, **26**(3), 347-364.

Li, X. P., Rahn, M., & Bucher, K. (2004). 'Serpentinites of the Zermatt-Saas ophiolite complex and their texture evolution'. *Journal of Metamorphic Geology*, **22**(3), 159-177.

Lorand, J. P., Luguet, A., Alard, O., Bezos, A., & Meisel, T. (2008). 'Abundance and distribution of platinum-group elements in orogenic lherzolites; a case study in a Fontete Rouge lherzolite (French Pyrénées)'. *Chemical Geology*, **248**(3), 174-194.

Lorand J.-P., Alard O. & Luguet A. (2010) 'Platinum-group element micronuggets and refertilization process in Lherz orogenic peridotite (northeastern Pyrenees, France)'. *Earth Planetary Science Letters* **289**, 298–310.

Luguet, A., Lorand, J. P., & Seyler, M. (2003). 'Sulphide petrology and highly siderophile element geochemistry of abyssal peridotites: A coupled study of samples from the Kane Fracture Zone (45 W 23 20N, MARK area, Atlantic Ocean)'. *Geochimica et Cosmochimica Acta*, **67**(8), 1553-1570.

Luguet, A., Lorand, J.P., Alard, O. and Cottin, J.Y., (2004). 'A multi-technique study of platinum group element systematic in some Ligurian ophiolitic peridotites, Italy'. *Chemical Geology*, **208**(1), 175-194.

Magott, R., Fabbri, O. & Fournier, M., (2016). 'Subduction zone intermediate-depth seismicity: Insights from the structural analysis of Alpine high-pressure ophiolite-hosted pseudotachylyte (Corsica, France)'. *Journal of Structural Geology*, **87**, 95–114.

Mallmann, G., & O'Neill, H.S.C., (2007). 'The effect of oxygen fugacity on the partitioning of Re between crystals and silicate melt during mantle melting'. *Geochimica et Cosmochimica Acta* **71**, 2837–2857.

Malvoisin, B., Chopin, C., Baronnet, A., Brunet, F., Bezacier, L., & Guillot, S. (2017). Fe–Ni-rich silicate aggregates formed after sulfides in high-pressure serpentinites. *Journal of Petrology*, **58**(5), 963-978.

Malvoisin, B., Chopin, C., Brunet, F. & Galvez, M. E. (2012), 'Low-temperature wollastonite formed by carbonate reduction: a marker of serpentinite redox conditions', *Journal of Petrology* **53**(1), 159–176.

Marschall, H.R. & Schumacher, J., (2014), 'Arc magmas sourced from mélange diapirs in subduction zones', *Nature Geoscience*, **5**, 862–867.

Mattauer, M., Proust, F., Etchecopar, A., (1977) 'Linéation ''a'' et mécanisme de cisaillement simple liés au chevauchement de la nappe des schistes lustrés en Corse', *Bull. Soc. Géol. Fr.*, **29** 841–847

Mattauer, M., Faure,M.,Malavieille, J., (1981). Transverse lineation and large-scale structures related to Alpine obduction in Corsica. *Journal of Structural Geology* **3**, 401–409.

McInnes, B. I., McBride, J. S., Evans, N. J., Lambert, D. D., & Andrew, A. S. (1999). Osmium isotope constraints on ore metal recycling in subduction zones. *Science*, **286**(5439), 512-516.

Meresse, F., Lagabrielle, Y., Malavieille, J. & Ildefonse, B. (2012), 'A fossil Ocean–Continent Transition of the Mesozoic Tethys preserved in the Schistes Lustrés nappe of northern Corsica', *Tectonophysics* **579**, 4–16.

Merlini, A.; Grieco, G. & Diella, V. (2009), 'Ferritchromite and chromian-chlorite formation in mélange-hosted Kalkan chromitite (Southern Urals, Russia)', *American Mineralogist* **94**(10), 1459–1467.

Miller, D. P., Marschall, H. R. & Schumacher, J. C. (2009), 'Metasomatic formation and petrology of blueschist-facies hybrid rocks from Syros (Greece): implications for reactions at the slab–mantle interface', *Lithos* **107**(1), 53–67.

Mitchell R.H. & Keays R.R. (1981) 'Abundance and distribution of gold, palladium and iridium in some spinel and garnet lherzolites: implications for the nature and origin of precious metal-rich intergranular components in the upper mantle'. *Geochim Cosmochim Acta* **45**:2425-2442

Molli, G., Tribuzio, R., Marquer, D., 2006. 'Deformation and metamorphism at the eastern border of the Tenda Massif (NE Corsica): a record of subduction and exhumation of continental crust'. *Journal*

of Structural Geology **29**, 1748–1766.

Mellini, M.; Rumori, C. & Viti, C. (2005), 'Hydrothermally reset magmatic spinels in retrograde serpentinites: formation of "ferritchromit" rims and chlorite aureoles', *Contributions to Mineralogy and Petrology* **149**(3), 266–275.

Mungall, J. E. (2002), 'Roasting the mantle: slab melting and the genesis of major Au and Au-rich Cu deposits', *Geology* **30**(10), 915–918.

Mungall J. E. & Brenan J. M. (2014) 'Partitioning of platinum-group elements and Au between sulfide liquid and basalt and the origins of mantle-crust fractionation of the chalcophile elements'. *Geochim Cosmochim Acta* **125**:265-289.

Mungall, J. E., Hanley, J. J., Arndt, N. T., & Debecdelievre, A. (2006). 'Evidence from meimechites and other low-degree mantle melts for redox controls on mantle-crust fractionation of platinum-group elements'. *Proceedings of the National Academy of Sciences*, *103*(34), 12695-12700.

Mukherjee, R.; Mondal, S. K.; Rosing, M. T. & Frei, R. (2010), 'Compositional variations in the Mesoarchean chromites of the Nuggihalli schist belt, Western Dharwar Craton (India): potential parental melts and implications for tectonic setting', *Contributions to Mineralogy and Petrology* **160**(6), 865–885.

Ohnenstetter, M. (1992). 'Platinum Group Element Enrichment in the Upper Mantle Peridotites of the Monte Maggiore Ophiolitic Massif (Corsica, France): Mineralogical Evidence for Ore-fluid Metasomatism, *Mineralogy and Petrology* **46**, 85–107

Padrón-Navarta, J. A., Sánchez-Vizcaíno, V. L., Hermann, J., Connolly, J. A., Garrido, C. J., Gómez-Pugnaire, M. T., & Marchesi, C. (2013). 'Tschermak's substitution in antigorite and consequences for phase relations and water liberation in high-grade serpentinites'. *Lithos*, **178**, 186-196.

Pagé, P., Barnes, S. J., Bédard, J. H., & Zientek, M. L. (2012). 'In situ determination of Os, Ir, and Ru in chromites formed from komatiite, tholeiite and boninite magmas: implications for chromite control of Os, Ir and Ru during partial melting and crystal fractionation'. *Chemical Geology*, **302**, 3-15.

Pagé, P., & Barnes, S. J. (2016). 'The influence of chromite on osmium, iridium, ruthenium and rhodium distribution during early magmatic processes'. *Chemical Geology*, **420**, 51-68.

Panseri, M., Fontana, E., & Tartarotti, P. (2008). 'Evolution of rodingitic dykes: Metasomatism and metamorphism in the Mount Avic serpentinites (Alpine Ophiolites, southern Aosta Valley)'. Ofioliti, **33**(2), 165–185.

Paton, C., Hellstrom, J., Paul, B., Woodhead, J. & Hergt, J. (2011), 'Iolite: Freeware for the visualisation and processing of mass spectrometric data', *Journal of Analytical Atomic Spectrometry* **26**(12), 2508–2518.

Patten, C., Barnes, S. J., Mathez, E. A., & Jenner, F. E. (2013). 'Partition coefficients of chalcophile elements between sulfide and silicate melts and the early crystallization history of sulfide liquid: LA-ICP-MS analysis of MORB sulfide droplets'. *Chemical Geology*, **358**, 170-188.

Peach, C. L., Mathez, E. A., & Keays, R. R. (1990). 'Sulfide melt-silicate melt distribution coefficients for noble metals and other chalcophile elements as deduced from MORB: Implications for partial melting'. *Geochimica et Cosmochimica Acta*, **54**(12), 3379-3389.

Peach, C. L., Mathez, E. A., Keays, R. R., & Reeves, S. J. (1994). 'Experimentally determined sulfide melt-silicate melt partition coefficients for iridium and palladium'. *Chemical Geology*, **117**(1-4), 361-377.

Pearson D. G., Irvine G. J., Ionov D. A., Boyd F. R., Dreibus G. E. (2004) 'Re–Os isotope systematics and platinum group element fractionation during mantle melt extraction: A study of massif and xenolith peridotite suites'. *Chemical Geology* **208**, 29–59

Penniston-Dorland, S. C., Gorman, J. K., Bebout, G. E., Piccoli, P. M. & Walker, R. J. (2014), 'Reaction rind formation in the Catalina Schist: Deciphering a history of mechanical mixing and metasomatic alteration', *Chemical Geology* **384**, 47–61.

Penniston-Dorland, S. C., Walker, R. J., Pitcher, L. & Sorensen, S. S. (2012), 'Mantle–crust interactions in a paleosubduction zone: Evidence from highly siderophile element systematics of eclogite and related rocks', *Earth and Planetary Science Letters* **319**, 295–306.

Peregoedova, A., Barnes, S. J., & Baker, D. R. (2004). 'The formation of Pt–Ir alloys and Cu–Pd-rich sulfide melts by partial desulfurization of Fe–Ni–Cu sulfides: results of experiments and implications for natural systems'. *Chemical Geology*, **208**(1-4), 247-264.

Puchtel, I.S., Humayun, M., Campbell, A.J., Sproule, R.A., Lesher, C.M., (2004), 'Platinum group element geochemistry of komatiites from the Alexo and Pyke Hills areas, Ontario, Canada', *Geochimica et Cosmochimica Acta*, **68**, 1361–1383.

Puchtel I.S., Humayun M. (2001) 'Platinum group element fractionation in a komatiitic basalt lava lake'. *Geochimica et Cosmochimica Acta* **65**, 2979–2993

Ravna, E., Andersen, T. B., Jolivet, L. & De Capitani, C. (2010), 'Cold subduction and the formation of lawsonite eclogite–constraints from prograde evolution of eclogitized pillow lava from Corsica', *Journal of Metamorphic Geology* **28**(4), 381–395.

Rielli, A., Tomkins, A. G., Nebel, O., Brugger, J., Etschmann, B., & Paterson, D. (2018). Garnet peridotites reveal spatial and temporal changes in the oxidation potential of subduction. *Scientific reports*, **8(**1), 16411.

Richards, J. P. (2009). Postsubduction porphyry Cu-Au and epithermal Au deposits: Products of remelting of subduction-modified lithosphere. *Geology*, **37**(3), 247-250.

Righter, K., Campbell, A. J., Humayun, M., & Hervig, R. L. (2004). 'Partitioning of Ru, Rh, Pd, Re, Ir, and Au between Cr-bearing spinel, olivine, pyroxene and silicate melts'. *Geochimica et Cosmochimica Acta*, **68**(4), 867-880.

Righter, K., & Downs, R. T. (2001). 'The crystal structures of synthetic Re-and PGE-bearing magnesioferrite Spinels: Implications for impacts, accretion and the mantle'. *Geophysical Research Letters*, **28**(4), 619-622.

Righter, K., & Hauri, E. H. (1998) ‘Compatibility of Re in garnet during mantle melting and magma genesis’, *Science* **280**:1737-1741

Roy-Barman, M., Wasserburg, G. J., Papanastassiou, D. A., & Chaussidon, M. (1998). ‘Osmium isotopic compositions and Re–Os concentrations in sulfide globules from basaltic glasses’. *Earth and Planetary Science Letters*, **154**(1-4), 331–347.

Salters, V. J., & Stracke, A. (2004). ‘Composition of the depleted mantle’. *Geochemistry, Geophysics, Geosystems*, **5**(5)

Savard, D., Barnes, S-J., & Meisel, T. (2010) ‘Comparison between Nickel-Sulphur Fire Assay Te Co-precipitation and Isotope Dilution with High-Pressure Asher Acid Digestion for the Determination of Platinum-Group Elements, Rhenium and Gold’, *Geostandards and Geoanalytical Research*, **34**, 281–291.

Scambelluri, M., Pettke, T., Rampone, E., Godard, M., & Reusser, E. (2014), 'Petrology and trace element budgets of high-pressure peridotites indicate subduction dehydration of serpentinized mantle (Cima di Gagnone, Central Alps, Switzerland)', *Journal of Petrology*, **55**(3), 459–498.

Scambelluri, M., & Tonarini, S. (2012). ‘Boron isotope evidence for shallow fluid transfer across subduction zones by serpentinized mantle’. *Geology*, **40**(10), 907-910.

Schwarzenbach, E.M., Früh-Green, G.L., Bernasconi, S.M., Alt, J.C., Shanks III, W.C., Gaggero, L. and Crispini, L., (2012). ‘Sulphur geochemistry of peridotite-hosted hydrothermal systems: comparing the Ligurian ophiolites with oceanic serpentinites’. *Geochimica et Cosmochimica Acta*, **91**, 283–305.

Schwarzenbach, E. M., Gazel, E., & Caddick, M. J. (2014). ‘Hydrothermal processes in partially serpentinized peridotites from Costa Rica: evidence from native copper and complex sulphide assemblages’. *Contributions to Mineralogy and Petrology*, **168**(5), 1079.

Seyler, M., Lorand, J. P., Dick, H. J., & Drouin, M. (2007). Pervasive melt percolation reactions in ultra-depleted refractory harzburgites at the Mid-Atlantic Ridge, 15 20′ N: ODP Hole 1274A. *Contributions to Mineralogy and Petrology*, **153**(3), 303.

Spandler, C., Hermann, J., Faure, K., Mavrogenes, J. A. & Arculus, R. J. (2008), 'The importance of talc and chlorite “hybrid” rocks for volatile recycling through subduction zones, evidence from the high-pressure subduction mélange of New Caledonia', *Contributions to Mineralogy and Petrology* **155**(2), 181–198.

Spandler, C. & Pirard, C. (2013), 'Element recycling from subducting slabs to arc crust: A review', *Lithos* **170**, 208–223.

Spear, F. S., 1981. ‘An experimental study of hornblende stability and compositional variability in amphibolite’. *American Journal of Science,* **281**, 697–734.

Sun, W., Bennett, V. C., & Kamenetsky, V. S. (2004). ‘The mechanism of Re enrichment in arc magmas: evidence from Lau Basin basaltic glasses and primitive melt inclusions’. *Earth and Planetary Science Letters*, **222**(1), 101-114.

Tribuzio, R., Giacomini, F., 2002. 'Blueschist facies metamorphism of peralkaline rhyolites from the Tenda crystalline massif (northern Corsica): evidence for involvement in the Alpine subduction event?' *Journal of Metamorphic Geology* **20**, 513–526.

Vitale Brovarone, A., Beltrando, M., Malavieille, J., Giuntoli, F., Tondella, E., Groppo, C., Beyssac, O. & Compagnoni, R. (2011), 'Inherited ocean–continent transition zones in deeply subducted terranes: insights from Alpine Corsica', *Lithos* **124**(3), 273–290.

Vitale Brovarone, A., Beyssac, O., Malavieille, J., Molli, G., Beltrando, M. & Compagnoni, R. (2013), 'Stacking and metamorphism of continuous segments of subducted lithosphere in a high-pressure wedge: the example of Alpine Corsica (France)'. *Earth-Science Reviews*, **116**, 35-56.

Vitale Brovarone, A. & Herwartz, D. (2013), 'Timing of HP metamorphism in the Schistes Lustrés of Alpine Corsica: New Lu–Hf garnet and lawsonite ages', *Lithos* **172**, 175–191.

Walker, R.J., Brandon, A.D., Bird, J.M., Piccoli, P.M., McDonough, W.F. & Ash, R.D., (2005). '^{187}OS–^{186}Os systematics of Os-Ir-Ru alloy grains from southwestern Oregon', *Earth and Planetary Science Letters* **230**, 211–226.

Warburton, J., (1986). 'The ophiolite-bearing Schistes lustrés nappe in Alpine Corsica: a model for emplacement of ophiolites that have suffered HP/LT metamorphism', *Memoirs of the Geological Society of America* **164**, 313–331.

Wood, S. A. (1987). Thermodynamic calculations of the volatility of the platinum group elements (PGE): the PGE content of fluids at magmatic temperatures. *Geochimica et Cosmochimica Acta*, *51*(11), 3041-3050.

Wylie, A. G.; Candela, P. A. & Burke, T. M. (1987), 'Compositional zoning in unusual Zn-rich chromite from the Sykesville District of Maryland and its bearing on the origin of" ferritchromit"', *American Mineralogist* **72**(3-4), 413–422.

FIGURE CAPTIONS

Figure 1: (a) Map showing the locations and *P-T* conditions of the field areas Serra di Pigno and Capu Corvoli on Cap Corse, Corsica (redrawn from Brovarone et al., 2011, 2013). **(b)** Field photo showing the juxtaposition of lithologies at Serra di Pigno. **(c)** Map of Serra di Pigno sample localities. **(d)** Map of Capu Corvoli sample localities (adapted from Lahondère, 1992).

Figure 2: Photomicrographs illustrating textural features in the samples. Py = pyrite, atg = antigorite, mt = magnetite, chl = chlorite, hz = heazlewoodite, pn = pentlandite, bal = balangeroite, ml = millerite, di = diopside, tlc = talc, ttn = titanate. The types of images are backscattered electron (bse),

reflected light (rfl) and cross polarised light (xpl). Rock types are abbreviated for serpentinite sample distal to other lithologies (distal), proximal to metagabbro and metaquartzite (proximal MGMQ) and proximal to metagabbro and calc schist (proximal MGCS). **(a)** Porous Cr-spinel with antigorite inclusions and an Fe-rich spinel and pyrite (py) 1 rim in CO13-55 (proximal MGMQ, bse) **(b)** Cr-spinel boudins with chlorite (chl) rims (xpl) **(c)** Pn1 grain in CO13-40 (distal) overprinted by atg2 on the rim (rfl) **(d)** Balangeroite veins associated with hz 1. **(e)** heazlewoodite grain with inclusions of mt1, overprinted by a later phase of antigorite (atg2) in CO13-31 (distal, bse). **(f)** Heazlewoodite grain with inclusions of millerite in CO13-31 (distal, bse) **(g)** pentlandite grain in CO13-21 (proximal MGMQ) with inclusions of magnetite (mt2) (bse). **(h)** pn2 overprinting earlier Cr-spinels and mt1 in CO13-33 (proximal MGMQ) (bse). **(i)** pn2 cut by larger laths of diopside in CO13-55 (proximal MGCS xpl). **(j)** euhedral grains of pn3 associated with atg3 in CO13-55 (proximal MGCS (xpl). **(k)** Pt-rich metal alloy on the rim of two heazlewoodite grains in CO13-31 (distal, bse). **(l)** Py1 grains in CO14-04 (talc schist) with inclusions of chromite and an iron hydroxide rim, which contains inclusions of pyrrhotite (po, rfl). **(m)** py2 grains with a talc2 rim in CO14-04 (talc schist, xpl). **(n)** py3 rims on large magnetite grains in CO14-03 (chlorite schist, rfl). **(o)** Pt-rich metal alloy towards the rim of py1 in CO14-04 (talc schist, bse).

Figure 3: Summary of sulphide and oxide parageneses for **(a)** Serra di Pigno samples and **(b)** Capu Corvoli samples throughout the subduction cycle through seafloor alteration, subduction, early exhumation and late exhumation. The line thickness represents relative mineral abundance. Full mineral parageneses can be found in Electronic Appendix 11 and 12.

Figure 4: Major element compositions of sulphides in all samples plotted on the ternary diagram Fe+S+(Ni+Cu+Co) (mol %). Small symbols represent feature mapping data. Large symbols represent EPMA data (Table 2).

Figure 5: Primitive upper mantle (PUM) normalised concentrations of HSE in **(a)** whole rock **(b)** heazlewoodite1 in CO13-31 (distal) **(c)** pentlandite2 in CO13-33 (proximal MGMQ) and pentlandite3 CO13-55 (proximal MGCS), and **(d)** pyrite2 in CO14-04 (talc schist) and pyrite3 in CO14-03 (chlorite schist). For comparison to pre-subduction protoliths in (a), whole rock HSE data is plotted for slow-spreading centre peridotite from the Kane Fracture Zone (KFZP; Alard et al., 2005), subducted serpentinites from La Corea, Cuba (LCP; Blanco-Quintero et al., 2011), serpentinised peridotite from the Internal Ligurides (ILP), Ligurian Alps (Luguet et al., 2003; 2004), and to assess lithological controls on HSE distribution, Zermatt-Saas gabbro (ZSG) and gabbro eclogite (ZSGE) HSE concentrations from Dale et al., (2009) and hybrid rinds (HR) from Penniston-Dorland et al., (2012; 2014) are shown. For comparison of sulphide data, in (b), (c) and (d), pyrrhotite and pentlandite data from the KFZ (KFZS; Alard et al., 2005), pentlandite and pyrrhotite data from the IL, Ligurian Alps (ILS; Luguet et al., 2003; 2004), and gabbro pyrrhotite/pyrite data (ZSGS) and gabbro eclogite pyrite (ZSGES) data from the Zermatt-Saas (Dale et al., 2009) are shown. Data is normalised to the PUM HSE concentrations of Becker et al. (2006) and Fischer-Gödde et al. (2010).

Figure 6: Activity-activity aO_2–aS_2 diagram at 2 GPa after Evans et al. (2017) for **(a)** Distal Serra di Pigno serpentinites, **(b)** Proximal Serra di Pigno serpentinites, and **(c)** Capu Corvoli hybrid rocks. The arrows indicate the evolution of the mineral assemblages in the samples throughout the subduction cycle from seafloor alteration, prograde metamorphism and exhumation.

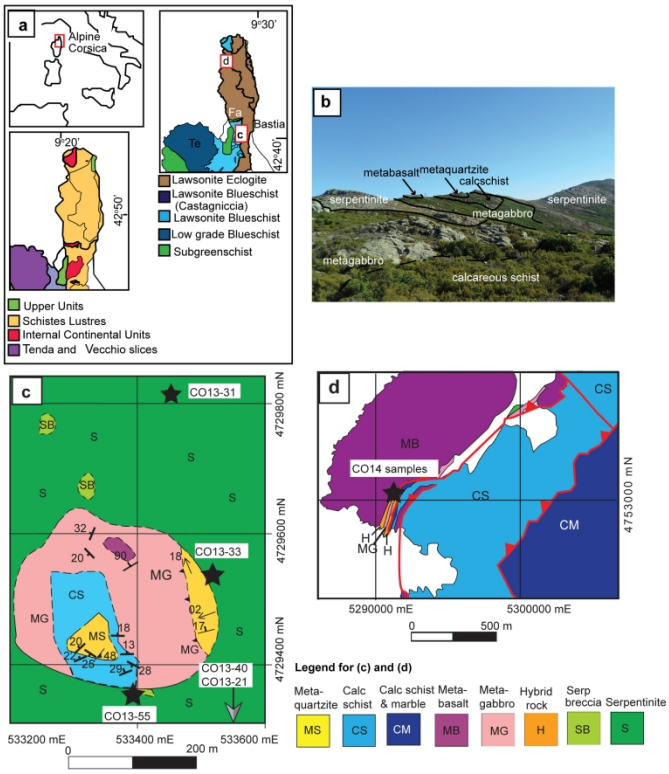

Figure 1: (a) Map showing the locations and P-T conditions of the field areas Serra di Pigno and Capu Corvoli on Cap Corse, Corsica (redrawn from Brovarone et al., 2011, 2013). (b) Field photo showing the juxtaposition of lithologies at Serra di Pigno. (c) Map of Serra di Pigno sample localities. (d) Map of Capu Corvoli sample localities (adapted from Lahondère, 1992).

210x296mm (300 x 300 DPI)

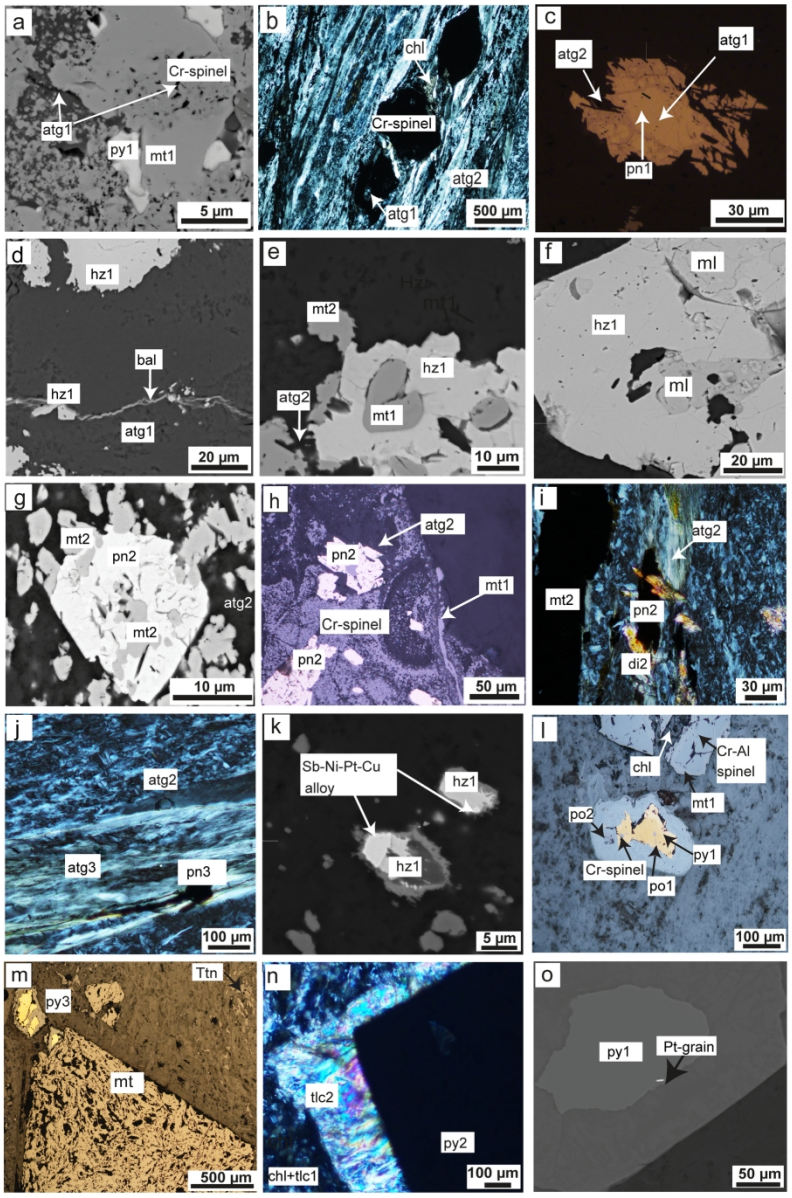

Figure 2: Photomicrographs illustrating textural features in the samples. Py = pyrite, atg = antigorite, mt = magnetite, chl = chlorite, hz = heazlewoodite, pn = pentlandite, bal = balangeroite, ml = millerite, di = diopside, tlc = talc, ttn = titanate. The types of images are backscattered electron (bse), reflected light (rfl) and cross polarised light (xpl). Rock types are abbreviated for serpentinite sample distal to other lithologies (distal), proximal to metagabbro and metaquartzite (proximal MGMQ) and proximal to metagabbro and calc schist (proximal MGCS). (a) Porous Cr-spinel with antigorite inclusions and an Fe-rich spinel and pyrite (py) 1 rim in CO13-55 (proximal MGMQ, bse) (b) Cr-spinel boudins with chlorite (chl) rims (xpl) (c) Pn1 grain in CO13-40 (distal) overprinted by atg2 on the rim (rfl) (d) Balangeroite veins associated with hz 1. (e) heazlewoodite grain with inclusions of mt1, overprinted by a later phase of antigorite (atg2) in CO13-31 (distal, bse). (f) Heazlewoodite grain with inclusions of millerite in CO13-31 (distal, bse) (g) pentlandite grain in CO13-21 (proximal MGMQ) with inclusions of magnetite (mt2) (bse). (h) pn2 overprinting earlier Cr-spinels and mt1 in CO13-33 (proximal MGMQ) (bse). (i) pn2 cut by larger laths of diopside in CO13-55 (proximal MGCS xpl). (j) euhedral grains of pn3 associated with atg3 in CO13-55 (proximal MGCS (xpl). (k) Pt-rich metal alloy on the rim of two heazlewoodite grains in CO13-31 (distal, bse). (l) Py1 grains in CO14-

04 (talc schist) with inclusions of chromite and an iron hydroxide rim, which contains inclusions of pyrrhotite (po, rfl). (m) py2 grains with a talc2 rim in CO14-04 (talc schist, xpl). (n) py3 rims on large magnetite grains in CO14-03 (chlorite schist, rfl). (o) Pt-rich metal alloy towards the rim of py1 in CO14-04 (talc schist, bse).

159x231mm (300 x 300 DPI)

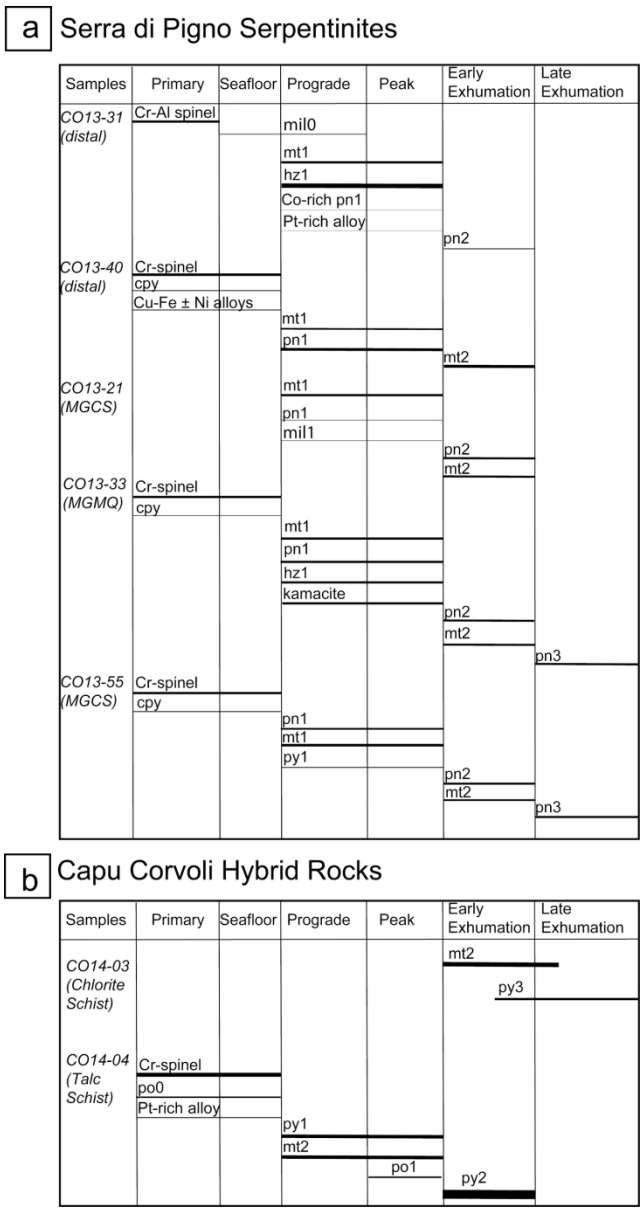

Figure 3: Summary of sulphide and oxide parageneses for (a) Serra di Pigno samples and (b) Capu Corvoli samples throughout the subduction cycle through seafloor alteration, subduction, early exhumation and late exhumation. The line thickness represents relative mineral abundance. Full mineral parageneses can be found in Electronic Appendix 11 and 12.

114x215mm (300 x 300 DPI)

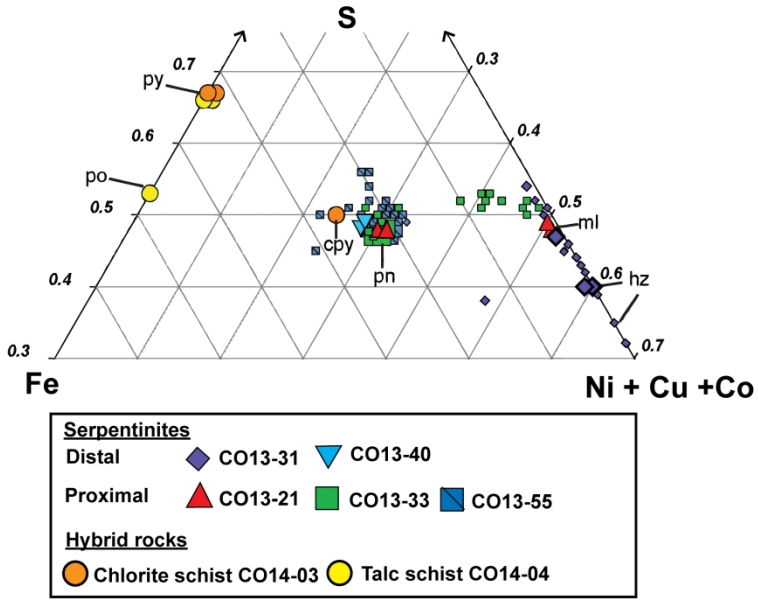

Figure 4: Major element compositions of sulphides in all samples plotted on the ternary diagram Fe+S+(Ni+Cu+Co) (mol %). Small symbols represent feature mapping data. Large symbols represent EPMA data (Table 2).

141x100mm (600 x 600 DPI)

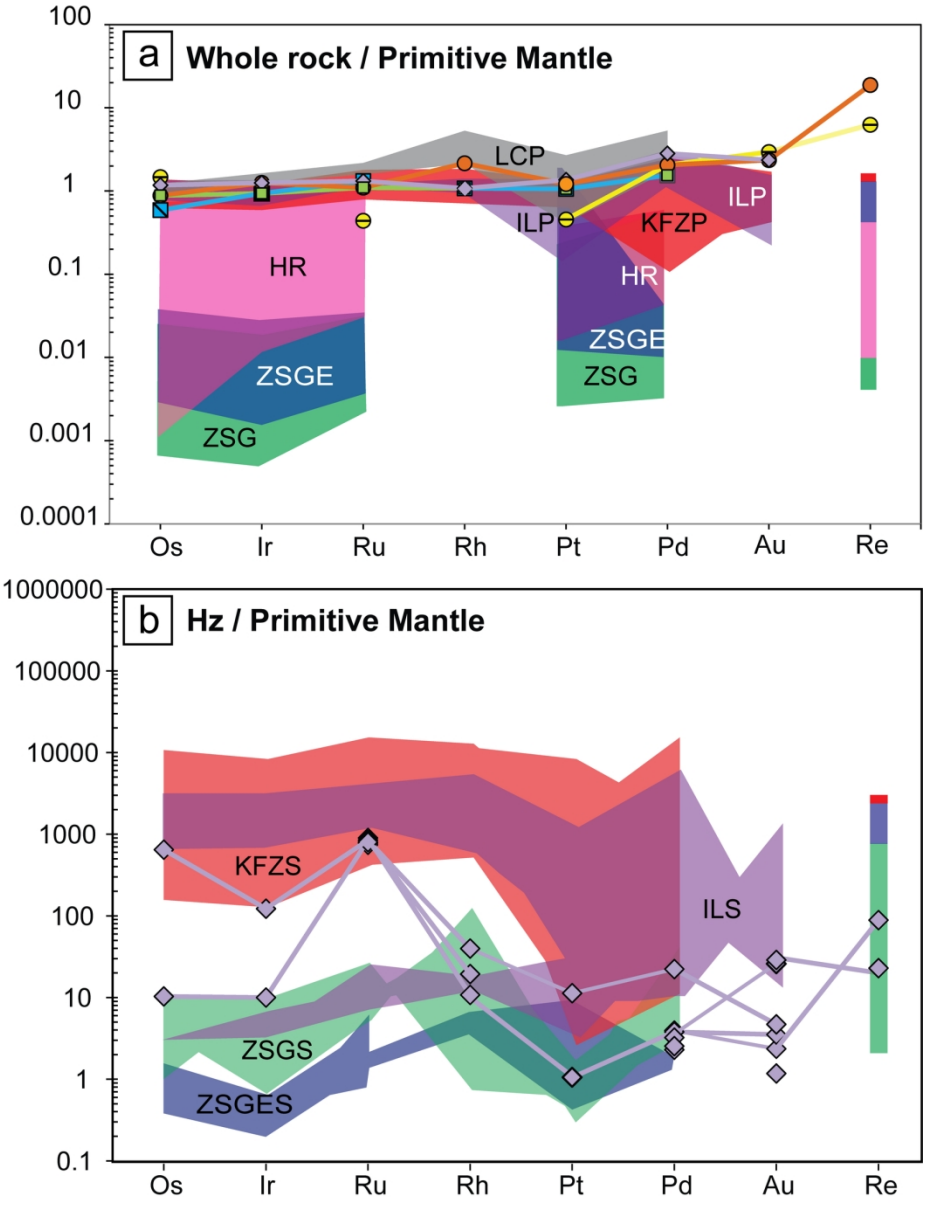

148x192mm (300 x 300 DPI)

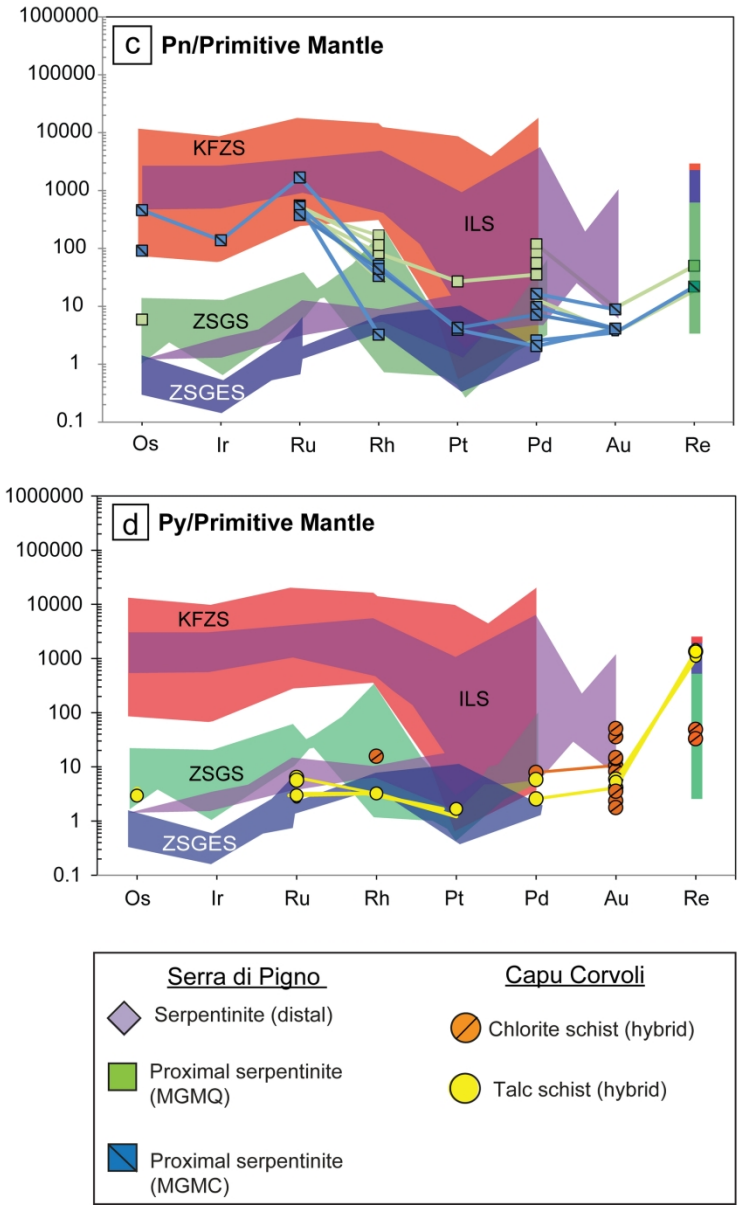

Figure 5: Primitive upper mantle (PUM) normalised concentrations of HSE in (a) whole rock (b) heazlewoodite1 in CO13-31 (distal) (c) pentlandite2 in CO13-33 (proximal MGMQ) and pentlandite3 CO13-55 (proximal MGCS), and (d) pyrite2 in CO14-04 (talc schist) and pyrite3 in CO14-03 (chlorite schist). For comparison to pre-subduction protoliths in (a), whole rock HSE data is plotted for slow-spreading centre peridotite from the Kane Fracture Zone (KFZP; Alard et al., 2005), subducted serpentinites from La Corea, Cuba (LCP; Blanco-Quintero et al., 2011), serpentinised peridotite from the Internal Ligurides (ILP), Ligurian Alps (Luguet et al., 2003; 2004), and to assess lithological controls on HSE distribution, Zermatt-Saas gabbro (ZSG) and gabbro eclogite (ZSGE) HSE concentrations from Dale et al., (2009) and hybrid rinds (HR) from Penniston-Dorland et al., (2012; 2014) are shown. For comparison of sulphide data, in (b), (c) and (d), pyrrhotite and pentlandite data from the KFZ (KFZS; Alard et al., 2005), pentlandite and pyrrhotite data from the IL, Ligurian Alps (ILS; Luguet et al., 2003; 2004), and gabbro pyrrhotite/pyrite data (ZSGS) and gabbro eclogite pyrite (ZSGES) data from the Zermatt-Saas (Dale et al., 2009) are shown. Data is normalised to the PUM HSE concentrations of Becker et al. (2006) and Fischer-Gödde et al. (2010).

156x245mm (300 x 300 DPI)

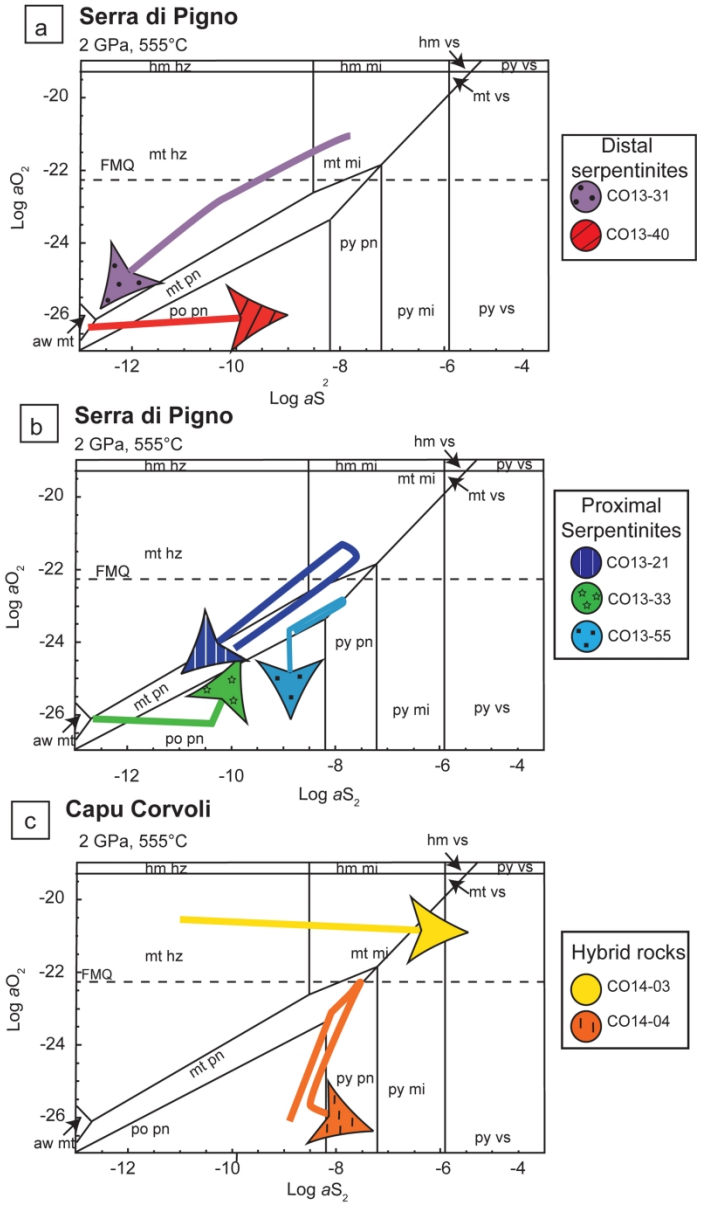

Figure 6: Activity-activity aO2–aS2 diagram at 2 GPa after Evans et al. (2017) for (a) Distal Serra di Pigno serpentinites, (b) Proximal Serra di Pigno serpentinites, and (c) Capu Corvoli hybrid rocks. The arrows indicate the evolution of the mineral assemblages in the samples throughout the subduction cycle from seafloor alteration, prograde metamorphism and exhumation.

142x245mm (300 x 300 DPI)

Table 1 Whole rock data, n.a. = not analysed, n.d. = not detected, < symbol followed by a number, represents concentrations less than the detection limit.

	CO13-31	CO13-40	CO13-21	CO13-33	CO13-55	CO14-03	CO14-04	CO14-05
wt%	*Serpentinites*					*Chlorite Schist*	*Talc Schist*	*Gabbro*
SiO_2	40.5	42.2	38.5	39.2	42.6	31.4	58.7	46.5
Al_2O_3	1.19	1.52	2.01	1.88	1.69	10.8	1.82	13.7
FeO	2.56	4.15	2.03	2.90	3.26	12.3	5.65	7.94
Fe_2O_3tot	6.54	9.09	7.07	8.98	6.42	20.4	8.48	12.3
MgO	39.0	36.4	38.7	38.4	37.7	17.9	24.8	7.45
CaO	0.03	0.16	0.06	0.04	2.04	4.97	0.03	9.94
Na_2O	0.13	0.11	0.13	0.09	0.14	0.10	0.03	1.76
K_2O	0.01	<0.01	0.01	<0.01	<0.01	<0.01	0.01	0.01
TiO_2	0.03	0.04	0.03	0.05	0.02	5.24	0.04	2.78
MnO	0.13	0.10	0.11	0.09	0.11	0.18	0.06	0.19
P_2O_5	<0.01	<0.01	<0.01	<0.01	0.02	0.09	0.01	0.11
LOI	11.7	11.2	12.1	11.6	10.7	7.24	5.45	5.13
Total	99.2	100.8	98.7	100.3	101.3	98.39	99.44	99.91
ppm								
C	200	200	200	300	200	200	300	570
S	300	300	700	1100	200	430	940	670
Cr	2245	2750	2470	2411	1812	621	2061	186
Co	103	113	130	114	99.2	123.1	85.2	45.5
Ni	2028	2287	2165	2254	2047	613	1579	89.6
Cu	3.10	n.a.	n.a.	8.40	4.30	24.3	18.5	105.4
Zn	39.0	63.0	37.0	40.0	32.0	92.0	56.0	67
Ga	1.80	2.60	2.90	2.10	2.70	19.90	3.70	17.4
As	<0.5	n.a.	n.a.	1.50	2.70	1.10	3.00	1.4
Se	<0.5	n.a.	n.a.	<0.5	<0.5	1.20	2.50	1.3
Mo	<0.1	<0.1	<0.1	<0.1	<0.1	0.10	<0.1	<0.1
Ag	<0.05	n.a.	n.a.	<0.05	<0.05	<0.05	<0.05	0.06
Cd	<0.02	n.a.	n.a.	<0.02	<0.02	0.03	<0.02	0.1
In	<0.01	n.a.	n.a.	0.01	<0.01	<0.01	<0.01	0.06
Sn	<1	<1	<1	<1	<1	2.0	<1	3
Sb	0.15	n.a.	n.a.	0.24	0.13	0.59	0.22	0.38
Te	<0.05	n.a.	n.a.	0.05	0.06	0.05	0.07	<0.1
Tl	<0.02	n.a.	n.a.	<0.02	<0.02	<0.02	<0.02	<0.02
Pb	1.10	n.a.	n.a.	1.10	0.70	0.80	0.60	<0.5
Bi	0.02	n.a.	n.a.	0.02	0.02	0.02	0.02	0.01
ppb								
Os	4	n.a.	n.a.	3	2	5	3	n.a.
Ir	4	n.a.	n.a.	3	3	<1	4	n.a.
Ru	6	n.a.	n.a.	5	6	2	5	n.a.
Rh	1	n.a.	n.a.	1	1	<1	2	n.a.
Pt	9	n.a.	n.a.	7	7	3	8	n.a.
Pd	11	n.a.	n.a.	6	6	8	8	n.a.
Re	<2	n.a.	n.a.	<2	<2	2	6	<2
Au	4	n.a.	n.a.	2	2	5	4	n.a.

Table 2: Average EPMA derived sulphide compositions (wt%). Number in brackets is two standard deviations. b.d.l indicates the concentration is below detection.

Sample	CO13-31	CO13-40	CO13-21	CO13-33	CO13-33	CO13-33	CO13-55	CO13-55	CO13-55	CO14-03	CO14-04	CO14-04
Phase	Hz1	Pn1 (n=10)	Pn1 (n=	Pn1 (n=6)	Pn2(n=14)	Pn3(n=10)	Pn1(n=9)	Pn2(n=8)	Pn3(n=13)	Py3(n=38)	Py1(n=21)	Py2(n=31)
wt%												
Si	0.04(3)	n.d.	0,1(2)	0.02(1)	0.04(3)	0.03(1)	0.05(3)	0.1(1)	0.04(4)	b.d.l	b.d.l	b.d.l
Mg	0.09(4)	n.d.	0,2(3)	0.09(9)	0.10(9)	0.05(4)	0.08(7)	0.07(4)	0.06(3)	b.d.l	b.d.l	b.d.l
Ni	73.2(5)	34(2)	41(11)	37.2(4)	37.1(3)	37.2(5)	37.5(8)	36(2)	37(1)	b.d.l	0.2(2)	0.2(2)
Fe	0.2(2)	28.4(7)	22(10)	25.3(4)	26.6(3)	26.1(5)	25.5(9)	26(1)	26(2)	45.3(5)	46.8(2)	46.8(4)
Co	<0.02	1.8(2)	1,8(8)	2.40(6)	2.32(5)	2.37(8)	2.3(2)	2.2(2)	2.3(2)	1.0(4)	0.1(3)	0.1(3)
S	27.0(1)	35(2)	33,1(3)	33.1(5)	33.3(3)	33.2(4)	33.4(2)	33.2(5)	33.3(2)	53.3(2)	53.9(3)	53.9(3)
Cu	0.058(3)	n.d.	b.d.l	0.01(1)	0.1(2)	0.01(1)	0.01(1)	0.010(3)	0.01(1)	b.d.l	b.d.l	b.d.l
Se	0.30(2)	n.d.	n.d.	0.15(1)	0.01(1)	0.14(2)	0.16(1)	0.16(1)	0.15(2)	n.d.	n.d.	n.d.
Bi	0.12(1)	n.d.	n.d.	0.12(1)	0.13(1)	0.13(1)	0.13(1)	0.120(4)	0.13(1)	n.d.	n.d.	n.d.
As	0.33(2)	n.d.	b.d.l	0.24(1)	0.22(2)	0.23(1)	0.27(4)	0.27(2)	0.25(3)	b.d.l	b.d.l	b.d.l
Sb	<0.02	n.d.	b.d.l	0.02(1)	0.01(1)	0.01(1)	0.02(1)	0.02(2)	0.02(1)	0.02(1)	0.02(1)	0.01(1)
TOTAL	101.5(5)	98.9(7)	98.1(5)	99(1)	99.2(5)	99.7(5)	99.5(7)	98.6(7)	98.7(5)	100.4(3)	101.1(3)	101.1(3)
mol%												
Ni	59.152(2)	26.9(8)	32.17(9)	29.27(7)	29.1(2)	29.1(3)	29.3(6)	28(1)	29(1)	-	0.1(1)	0.1(1)
Fe	0.188(1)	23.3(6)	18.52(8)	21.0(2)	21.1(2)	21.4(5)	20.9(7)	22(1)	21(1)	32.5(3)	33.2(1)	33.2(3)
Co	-	1.3	1.38(1)	1.88(5)	1.81(4)	1.85(6)	1.8(1)	1.7(1)	1.8(2)	0.7(3)	0.1(2)	0.1(1)
S	39.973(1)	49(1)	47.930(3)	47.8(2)	47.9(2)	47.5(3)	47.8(2)	47.9(3)	47.9(2)	66.79(9)	66.6(2)	66.6(2)
S/Fe+Ni+Co	0.67353(4)	0.94(5)	0.92(1)	0.92(1)	0.92(1)	0.91(1)	0.92(1)	0.92(1)	0.92(1)	2.011(8)	2.2(2)	2.2(3)

Table 3 HSE data for all sulphides (ppm). Standards include Po726 for PGE and Au, and Bon-NBS-6b for Re. <value reflects the detection limit.

	CO13-31 (distal)							*CO13-33 (MGMQ)*							*CO13-55 (MGCS)*
	s1	s2-2	s3_2	s4-4	s6-4	s7-4	s7-6	s1-2	s2-13	s2-18	s2-23	s3-2	s4-3	s4-8	s3-3
ppm	hz1	hz1	hz1	hz1	hz1	hz1	hz1	pn2	pn2	pn2	pn2	pn2	pn2	pn2	pn3
Os	2.19	<0.003	<0.012	<0.017	<0.025	0.035	<0.004	<0.012	<0.021	<0.041	<0.032	<0.030	<0.013	<0.050	<0.011
Ir	0.427	<0.002	<0.009	<0.005	<0.029	0.035	<0.003	<0.028	0	<0.006	<0.032	<0.003	<0.007	<0.008	<0.005
Ru	3.84	3.55	4.09	4.02	3.37	3.84	3.63	2.28	2.22	1.90	2.10	2.41	2.04	2.44	2.51
Rh	<0.018	0.003	0.01	<0.004	<0.005	0.037	<0.004	0.043	0.043	0.077	0.141	0.028	0.156	0.106	<0.003
Pt	<0.004	<0.005	<0.014	0.008	<0.014	0.086	<0.005	<0.020	<0.015	0.177	<0.021	<0.001	<0.007	<0.017	<0.009
Pd	0.028	0.016	0.026	0.025	0.023	0.158	0.018	0.184	0.458	0.138	0.227	0.051	0.310	0.217	0.033
Au	0.004	0.002	<0.013	0.006	0.044	0.049	0.008	<0.084	<0.014	<0.007	<0.017	<0.099	<0.038	<0.11	<0.005
Re	0.031	0	0	0.0018	<0.008	0.032	0.009	<0.005	0.016	<0.002	<0.002	<0.006	<0.002	<0.009	<0.007

CO13-55 (MGCS)					*CO14-03 (Chlorite Schist)*									
	s2-3	s1-3	s4-2	s4-3	s1-1	s1-2	s1-3	s1-4	s1-5	s1-6	s2-1	s2-2	s2-3	s2-4	s2-5
ppm	pn3	pn3	pn3	pn3	py3	py3	py3	py3	py3	py3	py3	py3	py3	py3	py3
Os	<0.041	<0.007	0.310	1.558	0	<0.005	<0.003	0	<0.007	<0.005	<0.003	0	<0.003	<0.004	<0.004
Ir	<0.018	<0.004	0	0.443	<0.001	<0.001	<0.0004	<0.001	<0.001	<0.001	0	<0.0004	<0.001	<0.001	<0.001
Ru	2.39	2.38	1.71	7.62	0.000	<0.001	<0.002	<0.002	<0.006	<0.002	<0.003	0.000	<0.004	<0.003	0.000
Rh	0.031	<0.005	<0.041	0.047	<0.004	<0.0005	<0.0009	<0.0007	<0.001	<0.001	0.015	0.001	<0.002	<0.002	0.004
Pt	<0.009	<0.014	<0.028	0.026	<0.002	<0.002	<0.002	<0.002	<0.002	<0.002	<0.003	<0.001	<0.004	<0.001	<0.004
Pd	0.055	0.007	<0.028	0.037	<0.002	<0.001	<0.003	<0.002	0	<0.001	0.031	<0.002	<0.003	0	0
Au	<0.015	<0.006	<0.007	0.191	0.003	0.003	0.004	0.061	0.003	0.006	0.018	0.047	0.004	0.006	0.014
Re	<0.01	<0.007	0	<0.004	0	<0.001	<0.003	<0.001	0.005	0.0157	0.003	<0.004	0.008	0.0105	<0.004

CO14-03 (Chlorite Schist)								*CO14-04(Talc Schist)*							
	s2-6	s2-7	s3-1	s3-2	s3-3	s3-4	s3-5	s1-1	s1-2	s1-3	s2-1	s2-2	s2-3	s3-1-1	s3-1-2
ppm	py3	py3	py3	py3	py3	py3	py3	py2	py2	py2	py2	py2	py2	py2	py2
Os	0	<0.003	<0.002	<0.003	<0.007	<0.005	<0.004	<0.004	0	0	<0.003	<0.007	<0.003	<0.012	0
Ir	<0.0005	<0.001	<0.001	<0.001	<0.002	<0.001	<0.001	0	0	<0.001	<0.001	<0.002	<0.002	<0.012	0
Ru	0	<0.005	<0.003	<0.001	<0.003	0	0	<0.003	0.012	0.003	0.014	0.006	0.009	0.002	0.029
Rh	<0.001	<0.002	<0.001	<0.001	0.002	0.001	<0.001	<0.002	<0.001	<0.0006	<0.001	<0.002	<0.001	<0.004	<0.003
Pt	<0.004	<0.003	<0.002	<0.004	<0.002	<0.001	<0.002	0	<0.003	<0.002	<0.004	<0.004	0	0	0
Pd	<0.001	<0.002	<0.003	0	0	0	<0.002	0	0	<0.003	<0.002	<0.004	0	<0.01	0.010
Au	0.024	0.003	0.003	<0.007	0.006	0.086	0.025	<0.002	0.003	<0.003	<0.004	0.003	<0.003	0.003	<0.007
Re	0.0105	0.005	0.004	<0.002	0	0.0045	<0.003	0.489	0.463	0.491	0.445	0.466	0.374	0.326	0.431

CO14-04 (Talc Schist)			
	s3-1-3	s4-1	s4-2
ppm	py2	py2	py2
Os	<0.005	<0.012	<0.01
Ir	<0.003	0	0
Ru	0.026	0.015	0.014
Rh	<0.001	<0.003	<0.003
Pt	<0.004	<0.008	<0.011
Pd	0.023	0	0
Au	<0.007	<0.01	<0.009
Re	0.503	0.321	0.43